4-22-2023

The Characterization of the SARS-CoV-2 Receptor Binding Domain Interaction with the Human ACE2 Receptor and Potential Small Molecule Inhibitors

Camryn Carter
University of Richmond, camryn.carter@richmond.edu

The Characterization of the SARS-CoV-2 Receptor Binding Domain Interaction with the Human ACE2 Receptor and Potential Small Molecule Inhibitors

By

Camryn Carter

Honors Thesis

Submitted to:

Chemistry Department

University of Richmond

Richmond, VA

April 22, 2023

Advisor: Dr. Carol A. Parish

Introduction

In December 2019, a novel coronavirus, severe acute respiratory syndrome coronavirus 2 (SARS-CoV-2), was identified in Wuhan, China after numerous patients experienced pneumonia symptoms, but existing medicinal treatments were ineffective.[1] The global spread of the SARS-CoV-2 virus caused an outbreak of the infectious disease, coronavirus disease 2019 (COVID-19), which was soon after declared a pandemic by the World Health Organization, referred to as the COVID-19 pandemic.[2] According to John Hopkins University, over 1,000,000 people have died from SARS-CoV-2 infection and about 104,000,000 cases have been confirmed in the United States (US).[3] An infection of the SARS-CoV-2 virus is caused by the virus spike protein binding with the human angiotensin-converting enzyme 2 (hACE2) receptor. The most common symptoms reported of this respiratory disease are a cough, fever, difficulty breathing, fatigue, headache, sore throat, loss of taste or smell, congestion, nausea, vomiting, and diarrhea. Patients with severe cases can experience dyspnea, hypoxemia, and progressive respiratory failure which can result in organ failure or other fatal conditions.[4] Groups over the age of 60 and/or those with pre-existing conditions can experience a higher rate of fatality.

The hACE2 receptors, located on the surface of human throat cells and lung epithelial cells, are SARS-CoV-2 targets.[5] The function of this receptor is to aid the regulation of the renin-angiotensin system (RAS), which modulates both blood pressure and extracellular volume.[6] The hACE2 receptor is an enzyme which converts the substrate angiotensin II to the active form. The active form, angiotensin I-7, acts as a vasodilator.[7, 8] The direct interaction between the SARS-CoV-2 spike protein and the hACE2 receptor causes viral infection.[9] SARS-CoV-2 contains spike-like projections of glycoproteins on its surface that are responsible for host infection. Specifically, the ectodomain of the SARS-CoV-2 virus consists of a subunit,

S1, which contains the receptor-binding domain (RBD) and the membrane-fusion subunit, S2.[10] The SARS-CoV-2 RBD consists of a section of amino acids that interact directly with the hACE2 receptor called the receptor binding motif (RBM).

To prevent SARS-CoV-2 infection or lessen the symptoms of COVID-19, scientists and researchers have developed vaccines, antivirals, and other therapeutics. In December of 2020, the United States Food and Drug Administration (FDA) issued emergency use authorization (EUA) for mRNA vaccines developed by Pfizer-BioNTech and Moderna, followed quickly by EUAs for the adenovirus (viral vector) vaccines developed by Johnson & Johnson and Astra-Zeneca.[11] These vaccines produced multiple antibodies to various regions of the SARS-CoV-2 spike protein, including antibodies that targeted the the SARS-CoV-2 RBD, which prevents host cell entry by prohibiting the virus from attaching and interacting with the hACE2 receptor.[12,13] Additionally, over the years, effective SARS-CoV-2 antiviral therapies have been developed and are continuing to be studied. These antivirals are able to inhibit SARS-CoV-2 enzymes such as the SARS-CoV-2 polymerase or the SARS-CoV-2 protease or inhibit SARS-CoV-2 viral entry into host cells. Remdesivir is a FDA approved antiviral that inhibits the SARS-CoV-2 RNA polymerase by terminating the production of the RNA chain.[14] Tocilizumab and baricitinib are also FDA approved antivirals, but are for hospitalized adults suffering with breathing complications.[15] Tocilizumab is a monoclonal antibody that inhibits interleukin 6 receptors and therefore improves the condition of patients suffering from cytokine storm syndrome.[16] Baricitinib is a Janus kinase inhibitor that inhibits the proinflammatory signal of several cytokines.[17] Essentially, this inhibitor prevents SARS-CoV-2 from interacting with the hACE2 receptor by interrupting the passage of SARS-CoV-2 into the target cells. Other antiviral drugs such as molunupiravir, ritonavir, etc. have been issued as EUA antivirals. Previously developed

vaccines and antivirals are extremely effective in reducing hospitalizations and deaths among vaccinated individuals.[19, 20]

Previous studies have researched the interaction between the SARS-CoV-2 RBD and the hACE2 receptor; such as developing crystal structures of the SARS-CoV-2 RBD and hACE2 complex, analyzing the binding affinity of this interaction, and evaluating the effects of SARS-CoV-2 RBD mutations.[21, 22] The characterization of the SARS-CoV-2 RBD is important for developing additional medicinal treatments. This is especially significant given that previously developed vaccines and medications can become ineffective due to SARS-CoV-2 mutations.

Due to the global spread of SARS-CoV-2, the virus is prone to mutations, allowing it to evolve over time. However, numerous studies have reported that the mutation of SARS-CoV-2 is relatively slow, with an estimated two mutations per month.[26, 27] Researchers believed that because of the slow mutation rate of SARS-CoV-2, the virus would not be able to evade the immune system. However, in 2020 and early 2021 there were reports of SARS-CoV-2 variants and COVID-19 cases where patients had chronic infections and symptoms. Variants containing multiple SARS-CoV-2 mutations that significantly increase the transmissibility of the virus, worsen the severity of COVID-19 symptoms, or decrease the effectiveness of previously developed vaccines, therapeutics, or public health/social measures are considered variants of concerns. As of 2023, the major variants of concern, as in variants that exhibit more than one of the characteristics previously mentioned, are Alpha (B.1.1.7), Beta (B.1.351), Gamma (P1), Delta (B.1.617.2), and Omicron (B.1.1.529).[28, 29] Table 1 contains more information pertaining to the SARS-CoV-2 major variants of concern.

Table 1. SARS-CoV-2 Major Variants of Concern. The name of the variant and the time it was detected is listed as well as the specific SARS-CoV-2 receptor binding domain mutations.

Variants	Time Detected	RBD Mutations
Alpha	Sept. 2020	N501Y
Beta	Oct. 2020	K417 N, E484K, N501Y
Delta	Dec. 2020	K417 N, L452R, T478K
Gamma	Jan. 2021	L452R, T478K
Omicron (B.1.1.529)	Nov. 2021	G339D, S371L, S373P, S375F, K417 N, N440K, G446S, S477 N, T478K, E484A, Q493 K/R*, G496S, Q498R, N501Y, Y505H

Most recently, the Omicron variant was detected in November of 2021 and, of the major variants of concern, has the most SARS-CoV-2 RBD mutations. Initial reports speculated that the increase in the SARS-CoV-2 RBD mutations in addition to the rapid increase in the number of COVID-19 cases could be attributed to enhanced binding affinity of the Omicron RBD. Now, as of 2023, Omicron and its subvariants are the predominant SARS-CoV-2 strain in the US. Figure 1 illustrates the Omicron RBD and the highlighted Omicron mutations. Notably, there were conflicting reports of the specific amino acid mutation at the position 493: Q493K or Q493R.

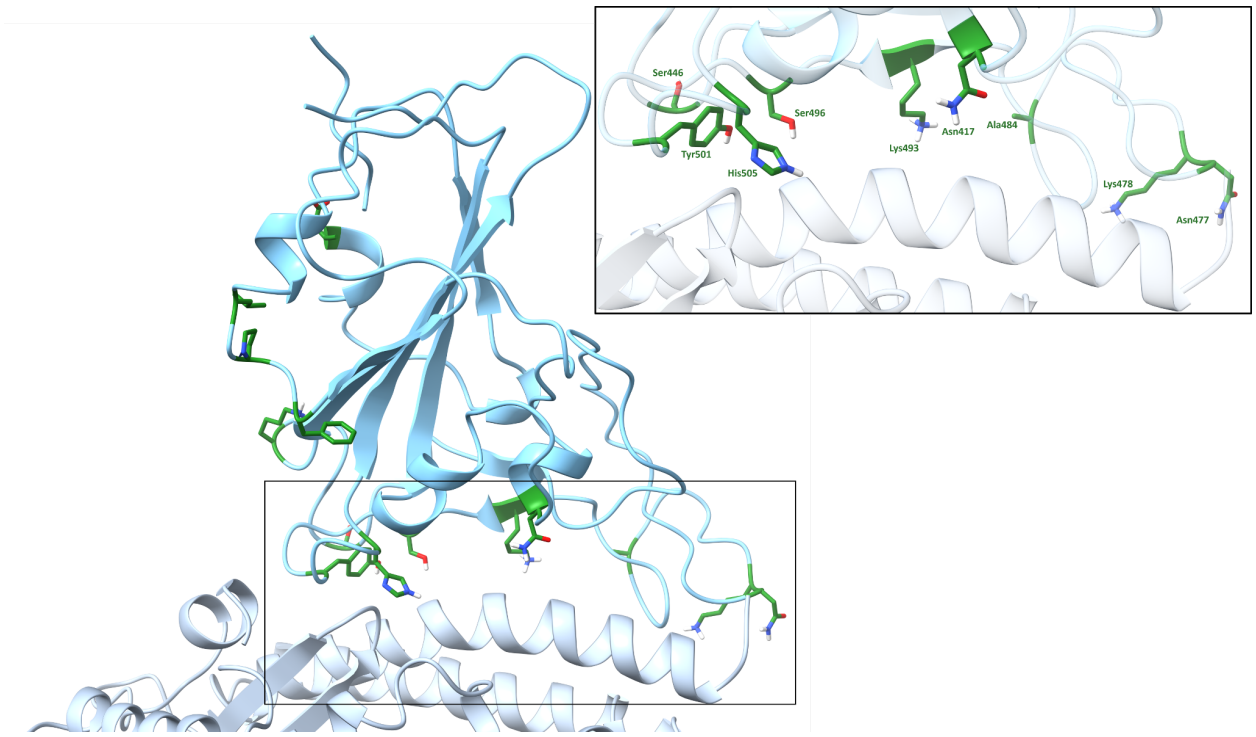

Figure 1. Omicron SARS-CoV-2 RBD - hACE2 Interaction. Omicron SARS-CoV-2 RBD is displayed in blue and hACE2 is displayed in a lighter blue. In green are the Omicron SARS-CoV-2 RBD residue mutations: G339D, S371L, S373P, S375F, K417N, N440K, G446S, S477N, T478K, E484A, Q493K, G496S, Q498R, N501Y, and Y505H. The binding site for the RBD - hACE2 interaction and the residues K417N, G446S, S477N, T478K, E484A, Q493K, G496S, N501Y, and Y505H are shown in the inset.

In the current study, we believed it was important to study the effect of the Omicron RBD mutations, specifically, how the mutations affected the structure and stability of the SARS-CoV-2 RBD, the binding affinity between the SARS-CoV-2 RBD and the hACE2 receptor, and the individual amino acid interactions responsible for said interaction. Previous experimental and computational studies have investigated the binding affinity of the Omicron RBD and compared the results to the wild type (WT) RBD.[30-38] Overall, we found that the results of previous studies were inconsistent, with various studies concluding that the Omicron RBD had an enhanced, decrease, or similar binding affinity compared to the WT RBD. Additionally, we recognized a pattern. Generally when researchers used an Omicron computational or experimental structure that contained the Q493K mutation, they concluded that the Omicron RBD has a less or similar

binding affinity to the WT RBD. Then when researchers used an Omicron computational or experimental structure that contained a Q493R mutation, generally they concluded that the Omicron RBD had an enhanced binding affinity. Table 2 illustrates the binding affinity results of previous studies and their conclusions. So, in this current study, we were interested in analyzing the effect of the mutation at position 493 on the RBD binding affinity.

Table 2. Previous Computational and Experimental Research Studies Focusing on Omicron and WT Binding Affinities. The experimental research studies measure the dissociation constant (K^D) and the binding affinity (K^{AFF}). The computational research studies estimate the binding free energy of the interaction. Additionally, the specific Omicron mutation at position 493 of the Omicron model used in the study is specified.

Model	K^D (nM)	Omicron Model	Ref.
WT	60 ± 1.4		Cameroni et al.[30]
	13.20		Zhang et al.[31]
	24.63 ± 5.00		Han et al.[32]
	22.0		Chan et al.[33]
	68.3		Cuit et al.[34]
Omicron	25.3 ± 1.2	Arg493	Cameroni et al.[30]
	8.85	Lys493	Zhang et al.[31]
	31.40 ± 11.62	Arg493	Han et al.[32]
	24.4	Arg493	Cui et al.[34]
Model	**K^{AFF} (L/mol)**	**Omicron Model**	**Ref.**
WT	$6.01 \pm 3.02 \times 10^7$		Wu et al.[35]
Omicron	$0.37 \pm 4.66 \times 10^7$	Lys493	Wu et al.[35]
Model	**Computational ΔG estimation (kcal/mol)**	**Omicron Model**	**Ref.**
WT	−33.13 ± 3.26		Wu et al.[35]
	−18.32 ± 1.62		Nguyen et al.[36]
	−32.43		Kumar et al.[38]
	−59.7		da Costa et al.[37]
	−29.43 ± 3.01	Lys493	Wu et al.[35]

Omicron	−30.21 ± 4.48	Arg493	Nguyen et al.[36]
	−41	Arg493	Kumar et al.[38]
	−75.4	Arg493	da Costa al. [37]

Lastly, we were interested in studying potential SARS-CoV-2 inhibitors by using preexisting small molecules and analyzing their effects on the interaction between the SARS-CoV-2 RBD and the hACE2 receptor. Previous studies have looked into screening small molecules in the SARS-CoV-2 RBD and hACE2 interface and studying the molecules' potential to inhibit the interaction.[23-25] However, in the current study we specifically focused on ACE inhibitors as potential SARS-CoV-2 inhibitors as well as pre-identified SARS-CoV-2 inhibitors. ACE inhibitors are used to treat cardiovascular and renal disease and are known to reduce hypertension and congestive heart failure. More information on these inhibitors are explained later on in the paper, but we decided to use ACE inhibitors as proof-of-concept potential SARS-CoV-2 inhibitors.

In this study, we found that the Omicron mutations do not have a significant effect on the SARS-CoV-2 RBD structure and stability. However, our results support that the Omicron RBD model containing the Q493R mutation has an increased binding affinity to the hACE2 receptor compared to both the WT and the Q493K Omicron RBD. Additionally, for both Omicron models we found that amino acid interactions between the SARS-CoV-2 RBD and the hACE2 receptor were lost, gained, strengthened, or decreased due to Omicron mutations. More detail is explained in this paper. Then from preliminary results of investigating potential SARS-CoV-2 inhibitors we found that ACE inhibitors would not be effective SARS-CoV-2 inhibitors based solely on binding affinity results. However, additional analyses are still being conducted.

Methods

Protein Retrieval and Preparation

An hACE2 - SARS-CoV-2 RBD crystal structure was obtained from the Protein Data Bank (PDB Code 6LZG).[39] Chains A (hACE2) and B (SARS-CoV-2 RBD) were selected from 6LZG, and all waters were removed. The Omicron structure was computationally constructed according to the 15 RBD point mutations mentioned in Table 1. Schrödinger's Protein Preparation Wizard was used to add missing hydrogen atoms, assign bond orders according to the CCD database, fill missing side chains using Prime, predict side chain protonation states using Epik with a pH range of 7 ± 2, and optimize H-bonds using PROPKA at a pH of 7.[40-42] Schrödinger's Protein Preparation Wizard was used to sample side chain conformers of amino acid residues Asn, Gln, His, Asp, and Glu during the optimization of H-bonding. Restrained minimization was then performed using the OPLS3e force field.[43]

Molecular Dynamics Simulations

Unrestrained classical molecular dynamics (cMD) was performed on the binary complex of SARS-CoV-2 RBD with hACE2 using the GPU-accelerated *pmemd* code of AMBER18.[44-46] The *ff*14SB and Glycam06j force fields were used to model standard amino acids, and glycosylated amino acids/glycans, respectively.[47, 48] The program *antechamber* was used to apply the GAFF force field and AM1-BCC charges to all ligands.[49, 50] All models were neutralized with Na^+ ions and explicitly solvated in a TIP3P unit cell using the program *tleap*.[44] A process of minimization, heating, and equilibration was performed prior to running unrestrained MD. Minimization occurred in seven stages of a maximum of 5000 steps each. The first 1000 steps consisted of steepest descent minimization and the remaining 4000 steps consisted of conjugate gradient minimization. An initial restraining force of 10.0 kcal mol^{-1} $Å^{-2}$ applied to the heavy

atoms of the solute was methodically decreased over the seven stages to 5.0, 2.0, 1.0, 0.5, 0.1, and lastly 0.0 kcal mol^{-1} $Å^{-2}$. Each structure was then heated linearly from 10 to 300 K while a restraining force of 10.0 kcal mol^{-1} $Å^{-2}$ was reapplied to all heavy atoms. Equilibration was then conducted in seven 500-ps stages, with the initial restraining force methodically decreased to 0.0 kcal mol^{-1} $Å^{-2}$ following the same procedure as that of minimization. Completion of equilibration was followed by a certain amount of randomly selected seeds depending on the Omicron study or the inhibitor study. A seed represents the initial protein ability to sample the potential energy surface and adapt different conformations. The seeds are randomized based on the different initial velocities of each starting structure, which is assigned in the heat step.

Molecular Dynamics Specification for RBD Comparison of WT and Omicron Models

Initially, 10 100 ns trajectories were generated for each model, each using different seeds to speed surface coverage. We concatenated the 10 seeds from each of the different SARS-CoV-2 RBD structures to obtain 1 μs ensembles for WT and the two Omicron binary complexes, initiated using the 6LZG experimental structure. We then extended these seeds by another 100 ns (200 ns total) and produced concatenated 2 μs ensembles for the all complexes.

Molecular Dynamics Specification for Potential SARS-CoV-2 Inhibitors

We generated 300 ns trajectories for each seed and concatenated the 10 seeds into a 3 μs ensemble for the apo complex (no ligand was bound). For the ligand bound MD simulations, we focused on 7 ligands with various poses which will be further discussed later in the paper. For each ligand bound complex with a distinct pose, we generated 100 ns trajectories for 5 seeds and the seeds were then concatenated into 500 ns ensembles.

Molecular Dynamics Analyses

Trajectory visualization was conducted using UCSF Chimera and UCSF ChimeraX.[61, 62] From this analysis we confirm that amino acid side chains sampled all possible rotamers as part of the cMD simulation. This is in addition to the rotamer analysis and screening that was performed as part of our initial protein preparation. Using the AmberTools *MMPBSA.py* package, MM-GBSA binding free energies and per-residue decomposition energies were calculated for every frame, and pairwise decomposition energies were obtained for frames at a 1 ns interval.[51] The GB^{OBC2} model (igb = 5) was used for the previously mentioned analyses. Native contact analysis, as defined by Best et al., was conducted on all trajectories between RBD and hACE2 heavy atom pairs.[63] MDTraj was used to calculate the native contacts in the interface. Hydrogen bonding, center-of-mass distance (COM), root-mean-squared deviation (RMSD), root-mean-square fluctuation (RMSF), secondary structure, backbone atom RMSD-based clustering, and non-hydrogen atom pairwise distance-based clustering analyses were conducted using the AmberTools *cpptraj* module.[51] Each clustering method resulted in 10 families per model.

SiteMap Analysis and Receptor Grid Generation

Schrödinger's SiteMap program was used to predict and score potential sites for ligand binding.[52] These potential sites are assigned both Site Scores (SScore) and Drugability Scores (DScore) based on volume, hydrophilicity/hydrophobicity, and H-bonding ability. Binding sites with a SScore of at least 0.8 and a DScore of at least 0.83 are likely to allow ligand binding.[52,56] Predicted binding sites are ranked based on size. SiteMap was run with default parameters on chains A and B of 6LZG. Five binding sites were identified, three of which returned favorable scores for 6LZG. Site #2, which was identified as a potentially favorable binding site, occurs at

the hACE2 - SARS-CoV-2 complex junction. Schrödinger's Receptor Grid Generation program was then used to generate a 40Å by 40Å by 40Å receptor grid with a ligand size cutoff of 20Å centered on Site #2 in both models. All parameters were kept at their default values. These receptor grids were used for all subsequent ligand docking.

Ligand Selection, Preparation, and Docking

Structures of common ACE inhibitors benazepril, captopril, enalapril, fosinopril, fosinoprilat, lisinopril, perindopril, quinapril, ramipril, and trandolapril were manually built and optimized according to the GAFF force field using Avogadro 1.2.[53, 54] Additionally, aloe emodin-LS-H15204, emodin-LS-H11074 and H17409, camostat-LS-H6976, and physcion-LS-H9395, identified by LSBio as potential SARS-CoV-2 Spike (S) Protein inhibitors and diquafosol, selected due to the phosphate groups, were also built using the same method detailed above. While this is not an expansive list, the goal of this study was simply to demonstrate that ligand binding to the site of interest is possible. Additionally, we want to explore how ACE inhibitors act as SARS-CoV-2 RBD inhibitors and compare them to other identified small molecules. Schrödinger's Empirical pKa Prediction (Epik) was used to predict the protonation states of each ligand at a pH of 7.4 ± 0.1. Schrödinger's Glide Docking program was used to dock each ligand into Site #2 as encompassed by the receptor grid. Glide assigns a GlideScore to each ligand based on predicted polar and nonpolar interactions within the receptor grid.[55, 56] Default parameters were used with the XP docking algorithm, in addition to specifying 5 predicted poses per ligand. Ligands were selected for further analyses based on the GlideScore. The GlideScore cutoff was -4.5 kcal/mol; however, fosinoprilat was selected due to the structural similarity to fosinopril and significant difference in GlideScore. Absorption, distribution, metabolism, and excretion (ADME) screenings were conducted on all ligands using

Schrödinger's QikProp Program. Results were generated using the default settings and properties that exceeded the 95% range of known drugs are reported in the results section. Additionally, Pan-assay interference compounds (PAINS) screenings were conducted on the selected ligands using the following sources: https://www.cbligand.org/PAINS/ and https://zinc15.docking.org/patterns/home/. The default settings were used for both screenings.

Results and Discussion

The following results and discussion section will be divided into two main sections: comparison of WT and Omicron binding affinities and the study of potential SARS-CoV-2 RBD inhibitors.

SARS-CoV-2 RBD Comparison of Binding Affinities

Our overarching goal of the first section is to compare the binding behavior of the RBD of the WT and Omicron models. When this work was first initiated in November 2021, there were no experimental structures of the Omicron RBD in either apo form, or bound to hACE2. Therefore, we built an Omicron RBD by making *in silico* mutations of the RBD using the WT SARS-CoV-2 RBD-hACE2 experimental structure (PDB: 6LZG). Our approach assumed that the 15 mutations present in the Omicron variant do not significantly change the conformation of the SARS-CoV-2 RBD, and that atomic relaxation via local minimization is enough to stabilize our *in silico* mutated structure.

While our current study was under review, experimental structures of the Omicron SARS-CoV-2 RBD complexed with the hACE2 receptor had become available, including the cryo-EM Omicron B.1.1.529 variant structure published by Guo et al (PDB: 7WSA).[57] We decided to compare our *in silico* Omicron structure to this cryo-EM Omicron structure by

superimposing both models. The 6LZG WT structure is composed of 796 residues compared to the 7WSA Omicron structure which contains 803 residues. The Omicron RBD of the 6LZG structure is 196 residues, with one residue accounting for the NAG (N-glycosylated) glycan bound to Asn343. Similarly, the 7WSA structure has a glycan bound to Asn343, but has 6 additional residues located at the beginning and end of the RBD structure (Pro330, Asn331, Ile332, Lys528, Lys529, and Ser530) that are not present in the 6LZG structure. In total, the RBD of the 7WSA structure is composed of 202 residues. The hACE2 receptor for 6LZG is composed of 599 residues, including the three NAG glycans bound to Asn53, Asn90, and Asn322. Compared to the 7WSA model, 6LZG has one additional residue located at the end of the hACE2 structure (Ala614); however, the hACE2 structure of the 7WSA model has three additional NAG glycans bound to Asn103, Asn432, and Asn546. In total, the 7WSA hACE2 structure is composed of 599 residues. Additionally, the 6LZG structure contains a Zn ion, unlike the 7WSA structure. The additional residues on both the 6LZG and 7WSA structures are not significantly close to the binding site, so we believe these structures have similar abilities in determining the binding ability of the Omicron RBD to the hACE2 receptor (Figure S1).

Additionally, the superimposition of 7WSA with our mutated 6LZG Omicron model shows that the model is structurally true to the experimental structure (Figures 2 and S1). There are additional residues on both the 6LZG and 7WSA structures, but they are well removed from the binding site. From this comparison, we believe that our results using 6LZG are representative of the results that would be obtained using the 7WSA structure, i.e. these structures have similar capacities for determining the binding ability of the Omicron RBD to the hACE2 receptor. With this result we decided to continue to use the *in silico* Omicron models for this current study.

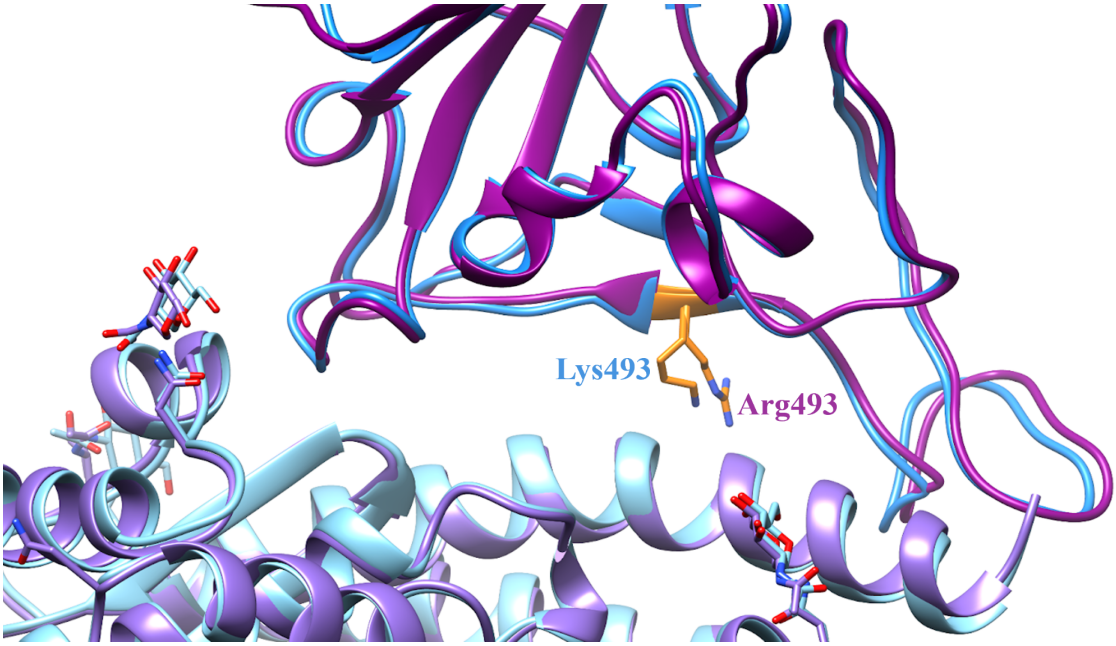

Figure 2. Comparison of the 6LZG and 7WSA Binding Sites. The 6LZG structure is in blue with the RBD depicted in dark blue and the hACE2 receptor depicted in light blue. The 7WSA structure is in purple with the RBD depicted in dark purple and the hACE2 receptor depicted in light purple. The Omicron mutation of the residue 493 is highlighted in orange on both structures. On the 6LZG WT structure residue 493 is a lysine and on the 7WSA Omicron structure this residue is an arginine. Both mutated residues have similar lengths and placement of the side chain conformers.

Using the WT structure (6LZG), as well as the *in silico* Omicron structures, we first performed 100 ns of MD simulations using 10 different, randomly selected, initial seeds. This generated 1 μs ensembles for each molecular system. We then extended these 10 seeds by another 100 ns each (for a total of 200 ns per seed) and conducted the same analyses on the resultant 2 μs ensembles. No significant differences in ensemble analyses were detected. As such, all further analyses were conducted on the 1 μs ensembles for computational efficiency, except where specified.

To assess conformational dynamics and simulation convergence, we computed the root-mean-squared-deviation (RMSD) of each ensemble conformation, relative to the corresponding initial structure. Overall, RMSD is measuring the average distance between the

position of atoms, which essentially is measuring the stability of the SARS-CoV-2 RBD and hACE2 complex. Figure 3 details the RMSD performed for all three models using the 2 µs ensemble. Apart from a brief increase in RMSD between 20 and 40 ns of WT seed 1, increased RMSD from 30 ns onwards in seed 5 of the Omicron Q493K model, and a brief increase in RMSD between 100 to 150 ns in seed 4 of the Omicron Q493R model, RMSD analysis shows that the WT and both Omicron complexes are relatively well converged across each seed, with RMSD values ranging from 2 to 3.5 Å. There are no significantly notable differences in the RMSD behavior of each model. This suggests thorough sampling of the dynamics of each complex and that the ensembles we are using to estimate binding free energy are conformationally converged. Additionally, because the RMSD behavior of each model is similar to one another this signifies that the models are sampling similar conformations, which further suggests that the models are comparable.

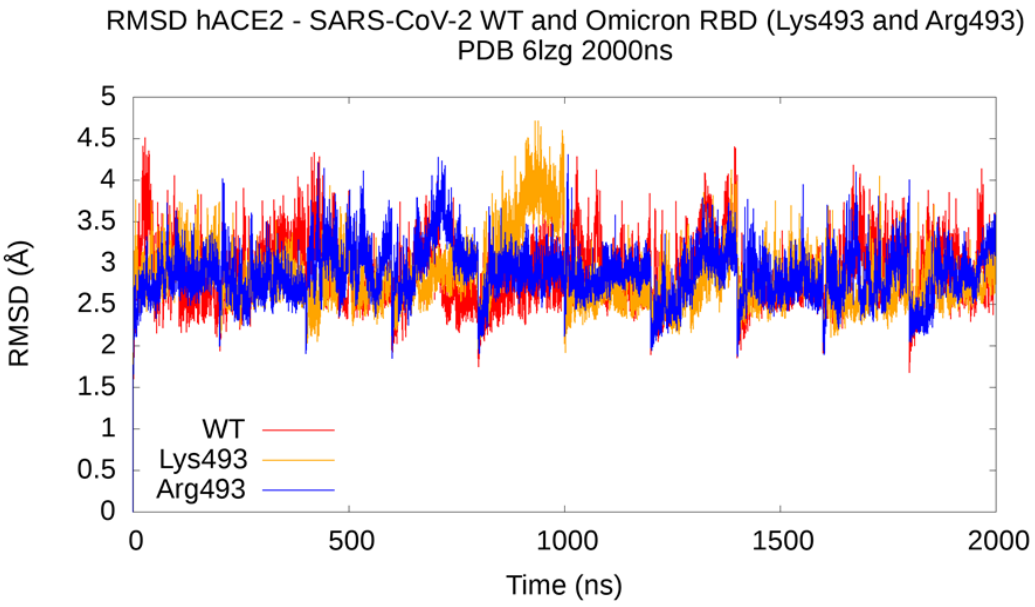

Figure 3. RMSD of SARS-CoV-2 RBD and hACE2 Models.

We also performed root-mean-square-fluctuation (RMSF) per residue analysis on each 1μs ensemble. RMSF measures the fluctuation or movement of every amino acid in the SARS-CoV-2 RBD and hACE2 complex. This analysis demonstrates that the fluctuations of the individual amino acids are also well conserved between seeds given the relatively low RMSF values for most of the structures. A comparison of the RMSF values for the WT and both Omicron models suggests relatively similar residue movements, with the exception of two amino acid ranges: 358 to 376 and 384 to 390. Figure 4 demonstrates the RMSF values for all three models in addition to the SARS-CoV-2 RBD structures. Notably, in the region 358 to 376 there are three Omicron mutations: S371L, S373P, and S375F. Additionally, in this residue range, there is an increase in the RMSF for the Omicron Q493R model. The residue range 384 to 390 does not contain any Omicron mutations and is far removed from the RBM, which is a region of SARS-CoV-2 RBD amino acids responsible for interacting with the hACE2 receptor. However, it is 10 residues away from the proline point mutation at position 373. This region, 384 to 390, is highlighted in Figure 4, with orange, red and yellow representing the region on the WT, Omicron Q493K, and Omicron Q493R models, respectively. Additionally, in this range, there is an increase in the RMSF for the Omicron Q493R model and there is a decrease in the RMSF for the Omicron Q493K model.

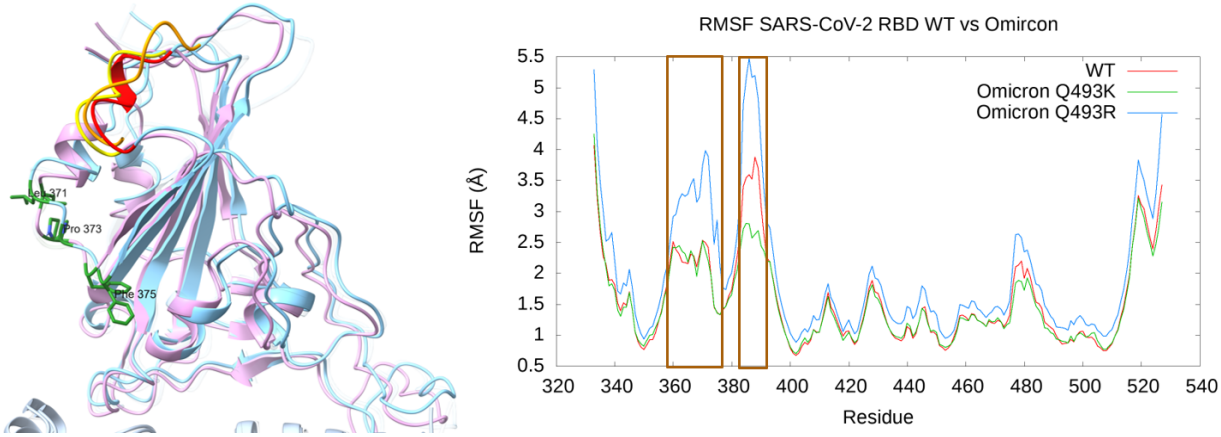

Figure 4. RMSF of SARS-CoV-2 RBD and hACE2 Models. On the left is a structure of the SARS-CoV-2 RBD of all three models. Additionally, the residue ranges 358 to 376 and 384 to 390 are encased in orange on the RMSF graph and are highlighted in orange, red, and yellow for the WT, Omicron Q493K, and Omicron Q493R, respectively.

To further explore why we see these differences in RMSF, we decided to conduct secondary structure analysis. Secondary structure analysis studies the change in secondary structure of amino acids across the simulation. Again in the residue range 358 to 376, there was an increase in the RMSF for the Omicron Q493R structure and this is further supported by the decrease in secondary structure seen in this range. Specifically, Figure 5 demonstrates that there is a decrease in the occurrence of alpha and 3-10 helices in the Omicron Q493R structure, where the frequencies for the WT, Omicron Q493K, and Omicron Q493R are as follows: 95.29, 94.26, and 87.71% respectively. This relatively small decrease in the helical occurrence can cause a decrease in the stability of the amino acid backbone atoms involved in the secondary structures; therefore, increasing the fluctuation of the amino acids. Then, as a reminder, Figure 4 demonstrates a decrease in the RMSF for the Omicron Q493K structure, but an increase in the RMSF for the Omicron Q493R structure. From secondary structure analysis and the average Omicron RBD structure, we found that there was a formation of a 3-10 helix involving the residues L387, N388, and D389 on the Omicron Q493K structure. Additionally, the percent occurrence of 3-10 helices in the WT, Omicron Q493K and Q493R are as follows: 4.25%, 69.26%, and 33.78% (Figure 6). This increase in the occurrence and formation of a 3-10 helix could have caused an increase in the stability of the amino acid backbones involved in the helix, thereby decreasing the amino acids' fluctuation. Additionally, to explain the increase in RMSF for the Omicron Q493R model in this range, we see the destabilization of two 3-10 helices throughout the simulation which can contribute to the increase in fluctuation of the amino acid backbones. In addition, there are predominantly more turn and bend structures compared to other

more stable secondary structures, which again can contribute to the fluctuation of the amino acids.

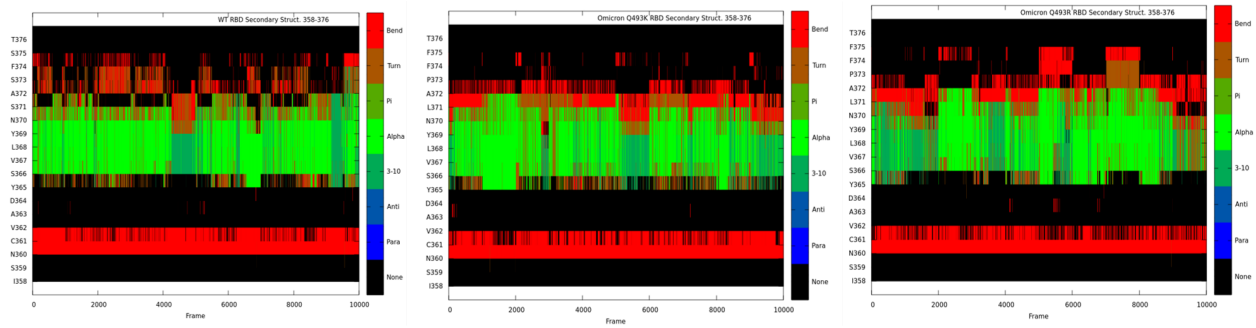

Figure 5. Secondary Structure Plots for Residue Range 358 to 376.

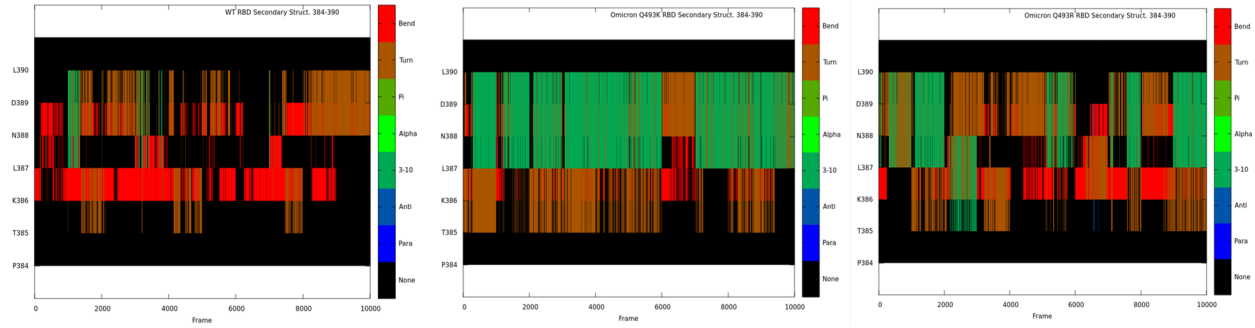

Figure 6. Secondary Structure Plots for Residue Range 386 to 390.

From RMSD, RMSF, and secondary structure analysis we found that the SARS-CoV-2 RBD and hACE2 complex is relatively stable for all three models. These analyses support that the Omicron mutations do not significantly affect the structure of the RBD, other than the few instances previously discussed. And most importantly, the Omicron mutations do not have a significant effect on the stability of the SARS-CoV-2 RBD interaction with the hACE2 receptor.

Then we focused on the binding affinity of the WT and Omicron RBD with the hACE2 receptor using MM-GBSA binding free energy estimations. Table 3 contains the binding free energies for all models and the corresponding concatenated ensemble time length. As shown in Table 3, the Omicron Q493K RBD has a similar/relatively decreased binding affinity compared

to the WT RBD. However, the Omicron Q493R RBD has a relatively enhanced binding affinity. This suggests that the Omicron Q493R RBD has a stronger interaction with the hACE2 receptor compared to the RBD of the other two models. These results are in agreement with previous computational and experimental studies that were discussed earlier. However, the current study conducted MM-GBSA analysis over all frames of the concatenated trajectory, while previous studies such as da Costa et al. and Kumar et al. conducted MM-GBSA analysis solely on the most stable structures and the last 10 ns of their trajectory, respectively.[37, 38] Therefore, our results provide a long time scale and more detailed atomistic view of the SARS-CoV-2 RBD binding affinity.

Table 3. MM-GBSA Binding Energies. The binding free energy estimations (kcal/mol) for the 1 and 2 μs ensembles of WT and Omicron SARS-CoV-2 RBD and hACE2 models.

Model	1 μs			2 μs		
	MM-GBSA Avg.	Std. Dev.	Std Error Mean	MM-GBSA Avg.	Std. Dev.	Std Error Mean
WT	-28.45	11.33	0.11	-29.69	10.61	0.07
Omicron (K493)	-25.61	7.57	0.08	-26.67	7.31	0.05
Omicron (R493)	-34.82	8.44	0.08	-34.56	8.24	0.06

First we studied the per-residue decomposition energies for the 2μs ensembles of all models to understand the role individual amino acids had on the SARS-CoV-RBD binding affinity. Per-residue decomposition energy is the energy a single amino acid contributes to the interaction between SARS-CoV-2 RBD and hACE2 receptor. Table S1 displays the most significant per-residue decomposition energies (less than -1 kcal/mol). The Omicron mutated amino acids are in red. Table S1 demonstrates that most per-residue decomposition energies are

similar across all three models and generally unmutated residues have relatively similar per-residue decompositions. However, there are a few notable differences in per-residue decomposition. Residue 449 remains a tyrosine in both WT and Omicron models, but there is a sizable decrease in the per-residue contribution (WT: -1.35 ± 1.00 kcal/mol, Omicron Q493K: -0.11 ± 0.32 kcal/mol, and Omicron Q493R: -0.15 ± 0.41). There are 8 unmutated residues that are significant for binding of both the WT and Omicron (Q493K and Q493R) RBD: F486F, F456F, Y489Y, L455L, G502G, N487N, A475A, and T500T.

Figure 7 highlights the per-residue decomposition energies of the 15 Omicron RBD mutated residues from WT (blue) to Omicron Q493K (orange) and Omicron Q493R (green). There are 4 mutated residues that are important for binding of both WT and Omicron (Q493K and Q493R) models: Q493K/R, G496S, N501Y, and Y505H; however, there is a noticeable decrease for Y505H (WT: -4.92 ± 0.98 kcal/mol, Omicron Q493K: -3.09 ± 1.32 kcal/mol, and Omicron Q493R: -3.33 ± 1.61). Additionally, there is a significantly favorable free energy contribution for the Omicron mutation N501Y (WT: -2.05 ± 1.19 kcal/mol, Omicron Q493K: -6.69 ± 1.17 kcal/mol, and Omicron 493R: -6.46 ± 1.15). The residue Q498 is significant for WT, and the 477N residue was significant only for the Omicron models, which is supported by a notable decrease in per-residue decomposition energy for the mutations Q498R (WT: -2.98 ± 3.21 kcal/mol, Omicron Q493K: -0.16 ± 1.26 kcal/mol, and Omicron Q493R: -0.30 ± 1.62 kcal/mol) and notable increase for the mutation S477N (WT: -0.31 ± 0.82 kcal/mol, Omicron Q493K: -1.10 ± 1.15 kcal/mol, and Omicron Q493R: -1.02 ± 1.17 kcal/mol), respectively. Table S1 and Figure 7 support that most per-residue decomposition energies are consistent across the three model, especially the pre-residue decomposition energies for both Omicron models;

however, there is a notable difference in per-residue contribution between the Q493K and Q493R mutations

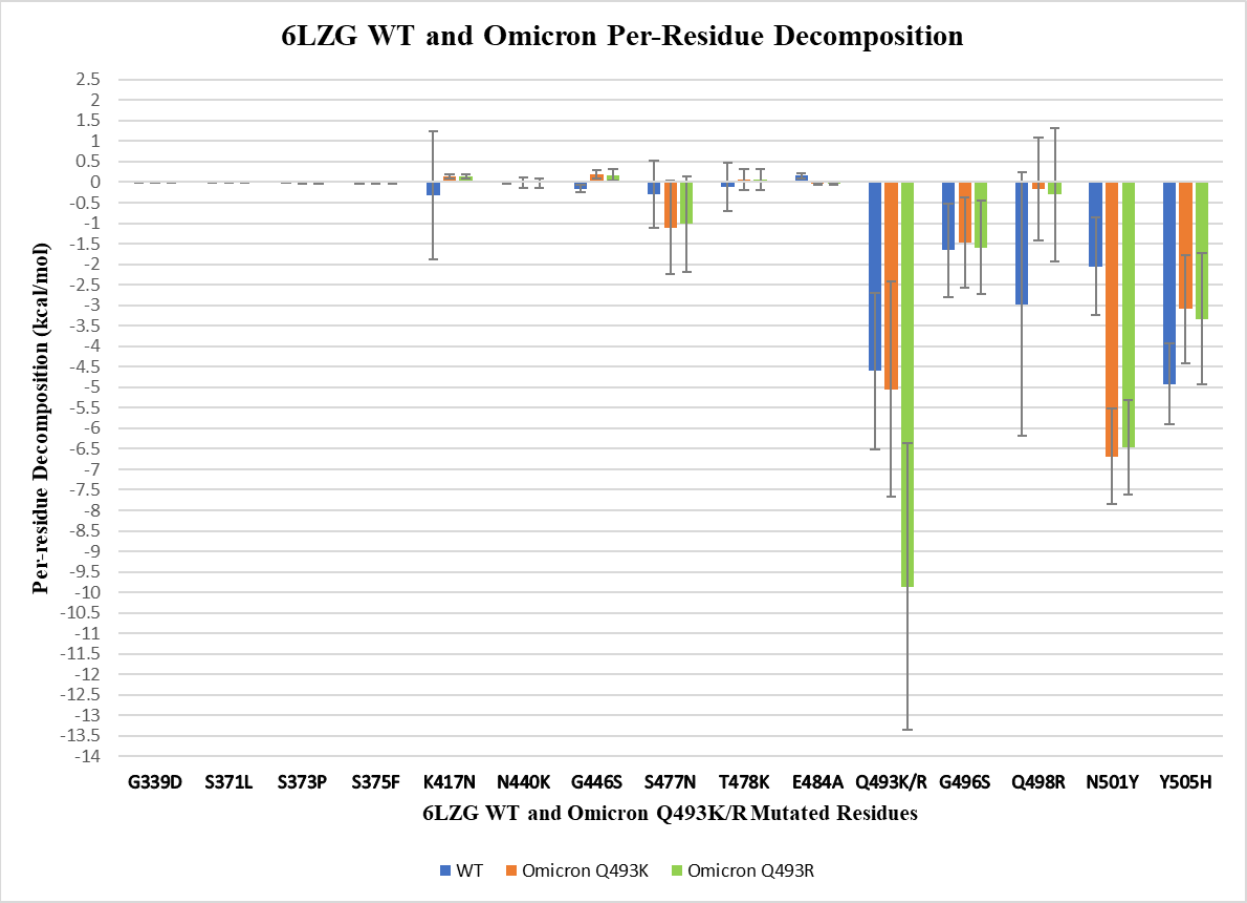

Figure 7. WT and Omicron Per-Residue Decomposition of SARS-CoV-2 RBD Mutated Residues. This bar graph demonstrates the per-residue decomposition energies for the 15 WT and Omicron (Q493K and Q493R) mutated RBD residues. The energies for WT are depicted in blue, the energies for Omicron Q493K are depicted in orange, and the energies for Omicron Q493R are depicted in green. Standard deviations are reported in black.

Table 4 contains the per-residue decomposition energies for the residues at position 493 in all three models. These energies suggest that not only does the residue at position 493 play a significant role in the binding between the SARS-CoV-2 RBD and hACE2 receptor, but possibly dictates the outcome of the binding affinity comparison. Specifically, the per-residue decomposition energies for the residues at position 493 on the WT and Omicron Q493K models

are very similar and based on the MM-GBSA results we concluded that the two models had similar binding energies. While the per-residue decomposition energy for R493 is significantly higher (more negative) than the other models. This not only further supports the enhanced binding affinity of the Omicron Q493R RBD, but, given the similarity in other residue energies between the two Omicron models, also suggests that a single point mutation causes the Omicron RBD to bind significantly tighter to hACE2 compared to the other two models.

Table 4. Per-residue Decomposition Energies for Residues at Position 493.

Model	Per-residue Decomp. (kcal/mol)	Std. Dev.	Std. Error Mean
WT (Q493)	-4.60	1.90	0.01
Omicron (K493)	-5.05	2.62	0.02
Omicron (R493)	-9.86	3.49	0.02

Additionally, to further support the estimated binding affinities of all three SARS-CoV-2 RBDs, we wanted to investigate the individual amino acid interactions and how they were affected by the Omicron mutations. Pairwise decomposition energies, which measure the energy of interaction for a pair of amino acids, were calculated for all three models. Our pairwise decomposition analysis is consistent with our MM-GBSA results in that it supports the relatively similarity in binding affinity to hACE2. Specifically, a summation of the energies of each favorable residue pair yields -54.68, -59.63, and -57.73 kcal/mol for the WT, Omicron Q493K, and Q493R models, respectively. Likewise, a summation of all pairwise interactions, both favorable and unfavorable, yields total energies of -117.53, -110.83, and -116.30 kcal/mol for the WT, Omicron Q493K, and Omicron Q493R models, respectively. Again, this further suggests

minimal differences in binding affinity across the models. Additionally, our data suggests that the main contributor to the different estimated binding affinities are the specific lost or gained amino acid interactions between the RBD and hACE2 receptor.

Table 5 illustrates that several pairwise interaction energies change upon mutation. Most notably, the Q493R/K mutation significantly increases binding, enhancing the strength of interaction with hACE2 residues His 34 and Glu 35, and providing a new interaction with hACE2 Asp38. While this disagrees with Geng et al., who reported that the Q493R mutation significantly reduced binding, several other studies agree with our findings.[34, 37, 38, 64] In the WT, neutral Gln493 contributes -4.84 and -4.10 kcal/mol when bound to hACE2 Glu35 and Lys31, respectively. However, the Omicron mutations to a positively charged Lys493 or a positively charged Arg493 creates very favorable interactions with hACE2 Glu35 (Omicron Q493K: -10.25 kcal/mol and Omicron Q493R: -12.65 kcal/mol) and with hACE2 Asp38 (Omicron Q493K: -8.09 kcal/mol and Omicron Q493R: -9.29 kcal/mol), while the interaction with hACE2 Lys31 is expectedly lost. In the WT, the S477 is not involved in a significant interaction, however in Omicron the S477N mutation creates an interaction with a binding energy contribution of -3.37 kcal/mol (Omicron Q493K) and -2.86 kcal/mol (Omicron Q493R) with hACE2 Ser19. Conversely, one of the strongest WT interactions between RBD Lys417 and hACE2 Asp 30 (-5.92 kcal/mol) is eliminated by the K417N mutation in Omicron. Similarly, the G496S and Q498R mutations result in lost interactions with hACE2 Lys353 (-3.07 and -3.00 kcal/mol respectively). Despite not being subjects of mutation, the WT interaction RBD Tyr449 – hACE2 Asp38 is also diminished in both Omicron models (Table 5).

Table 5. WT and Omicron SARS-CoV-2 RBD - hACE2 Pairwise Decomposition Energies. Pairwise decomposition energies that are more favorable (less) than -2.00 kcal/mol are listed. The pairwise decomposition energies are calculated from the full 1 μs ensemble and are reported

with the corresponding SARS-CoV-2 RBD and hACE2 residues. Omicron mutated residues are shown in red.

RBD WT Resid.	ACE2 Resid.	Pairwise Decomp. (avg. ± std. dev.) (kcal/mol)	RBD Omicron Q493K Residue	ACE2 Resid.	Pairwise Decomp. (avg. ± std. dev.) (kcal/mol)	RBD Omicron Q493R Residue	ACE2 Resid.	Pairwise Decomp. (avg. ± std. dev.) (kcal/mol)
Lys417	Asp30	-5.92 ± 3.34	Lys493	Glu35	-10.25 ± 3.21	Arg493	Glu35	-12.65 ± 4.42
Thr500	Asp355	-5.14 ± 2.38	Lys493	Asp38	-8.09 ± 3.61	Arg493	Glu38	-9.29 ± 5.22
Tyr505	Lys353	-5.06 ± 0.54	Thr500	Asp355	-6.44 ± 2.08	Tyr501	Lys355	-6.31 ± 0.94
Asn501	Lys353	-5.01 ± 1.47	Tyr501	Lys353	-6.38 + 1.00	Thr500	Asp355	-5.95 ± 2.24
Gln493	Glu35	-4.84 ± 1.62	His505	Lys353	-4.96 ± 1.45	His505	Lys353	-5.17 ± 1.41
Gln493	Lys31	-4.10 ± 2.04	Asn477	Ser19	-3.37 ± 2.68	Asn487	Gln24	-2.95 ± 0.93
Tyr449	Asp38	-3.26 ± 2.17	Asn487	Tyr83	-2.98 ± 0.89	Asn487	Tyr83	-2.93 ± 0.88
Gly496	Lys353	-3.07 ± 1.74	Arg498	Tyr41	-2.76 ± 0.70	Asn477	Ser19	-2.86 ± 2.71
Asn487	Tyr83	-3.02 ± 0.92	Asn487	Gln24	-2.75 ± 0.89	Ser496	Asp38	-2.79 ± 2.41
Gln498	Lys353	-3.00 ± 3.33	Lys493	His34	-2.61 ± 1.41	Arg498	Tyr41	-2.66 ± 0.71

Asn487	Gln24	-2.99 ± 0.90	Ala475	Ser19	-2.46 ± 1.54	Arg493	His34	-2.47 ± 1.67
Tyr505	Glu37	-2.59 ± 2.37	Phe486	Met82	-2.35 ± 0.79	Phe486	Met82	-2.35 ± 0.75
Phe486	Met82	-2.50 ± 0.81	Tyr489	Lys31	-2.16 ± 0.67	Tyr489	Lys31	-2.21 ± 0.75
Asn501	Tyr41	-2.13 ± 1.21	Ser496	Asp38	-2.05 ± 2.40			
Gln493	His34	-2.05 ± 1.34						

Interactions unaffected or preserved by mutation are also observed. The Q493K/R mutation does not disrupt the favorable interaction with His34 in the WT. The mutation Y505H does not seem to affect binding. In both the WT and Omicron RBDs, residue 505 interacts similarly with hACE2 residue Lys353 (WT: -5.06 kcal/mol; Omicron Q493K: -4.96 kcal/mol; Omicron Q493R: -5.17 kcal/mol), while the interaction with Glu37 doesn't change significantly with respect to standard deviation. Important interactions not subject to mutation, RBD Thr500 – hACE2 Asp355, RBD Asn487 – hACE2 Tyr83, RBD Asn487 - hACE2 Gln24, and RBD Ala475 – hACE2 Ser19, are unchanged between the WT and Omicron models. (Table 5).

Lastly we wanted to explore hydrogen bonding interactions that take place in the interface between SARS-CoV-2 RBD and the hACE2 receptor. Based on hydrogen bonding analysis, there is a decrease in the number of significant (defined as occurring for more than 5% of the ensemble) hydrogen bonding interactions between RBD and hACE2 residues upon Omicron mutation (Table 6). One interaction that is present in both WT and Omicron is the

hydrogen bond with the residue Q493K/R to the hACE2 residue Glu35 (WT: 68.16%, -4.84 ± 1.62; Omicron Q493K: 66.05%, -10.25 ± 3.21; Omicron Q493R: 66.44% and 33.29%, -12.65 ± 4.42). Notably, Omicron Q493R has two distinct interactions between the residues Arg493 and Glu35. We believe this is because Arg has more potential hydrogen bond donors compared to both Lys and Gln. Kumar et al. reported this interaction as important but occurring to a lesser extent (WT: 38.20% and Omicron Q493R: 11.10%).[38] For the WT model, there are seven more hydrogen bonds between RBD and hACE2 that also occur in the Omicron models. (Table 6). Notably, these interactions are between non-mutated RBD residues for WT and both Omicron models. The interaction RBD Thr500 – hACE2 Tyr41 appears to be significant for both WT and Omicron but there is a notable difference in hydrogen bonding occurrence (WT: 29.74 %, Omicron Q493K: 10.26%, and Omicron Q493R: 12.10%). In comparison, Kumar et al. reports that the RBD Thr500 – hACE2 Tyr41 interaction is only significant for the WT, occurring 18.40%. Also, Table 6 shows that the interactions RBD Tyr489 - hACE2 Tyr83, and RBD Tyr495 – hACE2 Lys353 are significant hydrogen bonding interactions for the WT but are not significant interactions for the Omicron models. The interaction RBD Tyr449 - hACE2 Asp38 appears to be significant for WT and the Omicron Q493R model, but there is a significant decrease in hydrogen bonding occurrence. Similarly, Kumar et al. saw a significant decrease in hydrogen bonding occurrence for RBD Tyr449 - hACE2 Asp38 (WT: 70.50% and Omicron: 17.10%); however, the RBD Tyr489 - hACE2 Tyr83 and RBD Tyr495 – hACE2 Lys353 were not significant interactions for their WT model. These discrepancies are likely due to significant differences in the simulation time, i.e analysis conducted over 1 μs in this study versus sampling hydrogen bonding over only 100ns in the Kumar et al study.[38]

Table 6. WT and Omicron SARS-CoV-2 RBD - hACE2 Hydrogen Bonding Occurrences. Individual hydrogen bonding percentages were combined for interactions between the same

residues and rotationally equivalent atoms on each residue. For example, the hydrogen bonding interactions between RBD Lys 493 and ACE2 Asp 38 (62.53%) are comprised of individual interactions between OD1 and OD2 with N-H1, N-H2 and N-H3. Unless specified, these consist of sidechain - sidechain interactions. Hydrogen bonding percentages that are greater than 5% are listed. In red are SARS-CoV-2 mutated residues.

RBD WT Residue	**hACE2 Residue**	**H-Bond % Occur. (Avg.)**	**RBD Omicron Q493K Residue**	**hACE2 Residue**	**H-Bond % Occur. (Avg.)**	**RBD Omicron Q493R Residue**	**hACE2 Residue**	**H-Bond % Occur. (Avg.)**
Asn487	Tyr83	83.27	Asn487	Tyr83	72.75	Asn487	Tyr83	61.16
	Gln24	23.27		Gln24	14.15		Gln24	14.60
Gly502	Lys353	77.58	Thr500	Asp355	67.49	Thr500	Asp355	52.58
Gln493	Glu35	68.07		Tyr41	10.26		Tyr41	12.10
	His34	7.66	Lys493	Glu35	66.05	Arg493	Asp38	74.21
	Lys31	42.66		Asp38	62.53		Glu35 Sidechain	66.44
Tyr449	Asp38	62.55	Gly502	Lys353	57.00		Glu35 Sidechain	33.29
Lys417	Asp30	62.26	Ala475	Ser19 Sidechain	38.27	Ala475	Ser19 Sidechain	32.79
				Ser19 Backbone	16.28		Ser19 Backbone	13.98
Thr500	Asp355	58.69		Gln24	5.28	Gly502	Lys353	51.59
	Tyr41	29.75	Ser496	Asp38	38.20	Ser496	Asp38	41.38
Tyr505	Glu37	49.41	Asn477	Ser19 Backbone	28.22	Asn477	Ser19 Backbone	22.90
				Ser19 Sidechain	11.42		Ser19 Sidechain	9.88
	Ala386	7.21	Tyr453	His34	19.68	Tyr453	His34	20.52
Gln498	Lys353	35.95	Arg498	Gln42	12.77	Arg498	Gln42	13.57
	Asp38	24.17					Asp38	5.81
Ala475	Ser19 Sidechain	31.34				Tyr449	Asp38	10.25
		5.85						

	Ser19 Backbone							
	Gln24	7.60						
Gly496	Lys353	30.70						
Tyr453	His34	24.79						
Tyr489	Tyr83	8.29						
Tyr495	Lys353	9.32						
Gly446	Gln42	8.17						

Additionally, we analyzed the pairwise and hydrogen-bonding data for all RBD mutated residues regardless of their values. Significant hydrogen bonding interactions of the WT RBD with hACE2 (RBD Lys417 – hACE2 Asp30, RBD Gly446 – hACE2 Gln42, RBD Gln493 – hACE2 Lys31, RBD Gly496 – hACE2 Lys353, RBD Gln498 – hACE2 Asp38, RBD Gln498 – hACE2 Lys353, RBD Tyr505 – hACE2 Glu37, and RBD Tyr505 – hACE2 Ala386) appear to be destroyed or diminished upon residue mutation in the Omicron variant. Notably, such residue mutations do not seem to introduce many new hydrogen bonding interactions, and as such, relative to the WT model, the Omicron mutations reduce hydrogen bonding occurrences more than they increase it.

However, the mutated RBD residues Asn477, Lys493/Arg493, Ser496, and Arg498 participate in significant hydrogen bonding interactions: RBD Asn477 – hACE2 Ser19, RBD Lys493/Arg493 – hACE2 Asp38, RBD Ser496 – hACE2 Asp38, and RBD Arg498 – hACE2 Gln42. However, the WT interaction RBD Gly496 – hACE2 Asp38 and Omicron interaction RBD Ser496 – hACE2 Asp38, both have relatively high pairwise decomposition values (WT: -0.86 ± 0.85 kcal/mol, Omicron Q493K: -2.05 ± 2.40 kcal/mol, and Omicron Q493R: -2.79 ±2.41 kcal/mol). The Omicron Q493K hydrogen bonding interactions RBD Ser496 – hACE2 Lys353, RBD Arg498 – hACE3 Asp38, and RBD His505 – hACE2 Glu37, appear to have low

hydrogen bonding occurrences compared to the equivalent WT interactions (with Omicron percent occurrences less than 5%); however, the pairwise decomposition values of these interactions are significant (Table 5) The Omicron Q493R hydrogen bonding occurrences for the previously mentioned hydrogen bonding interactions are similar to the Omicron Q493K model.

Overall, MM-GBSA estimations, per-residue and pairwise decomposition energies, and hydrogen-bonding interactions indicate three very important Omicron mutations: Q493K/R, N501Y and S477N. Strikingly, for Q493K, hACE2 binding to the WT and Omicron are similar, whereas for the Q493R RBD, Omicron binds more tightly. This is in agreement with previous experimental reports, using the Q493K RBD, that suggests Omicron binds similar or less tightly than WT,[32, 65] and also in agree with computational and experimental reports that suggests Omicron binds more tightly.[37, 38, 64] It is remarkable that a single point mutation can confer such differences in binding and it is imperative to experimentally test this computational prediction. The overall atomistic picture that emerges from our detailed study is that some of the mutations in the SARS-CoV-2 RBD and hACE2 interface enhance binding and that some of those enhancements are balanced by mutations that disfavor binding. The mutations that have the most significant effect on binding are shown in Figure 8, where favorable and unfavorable point mutations are shown in green and red, respectively.

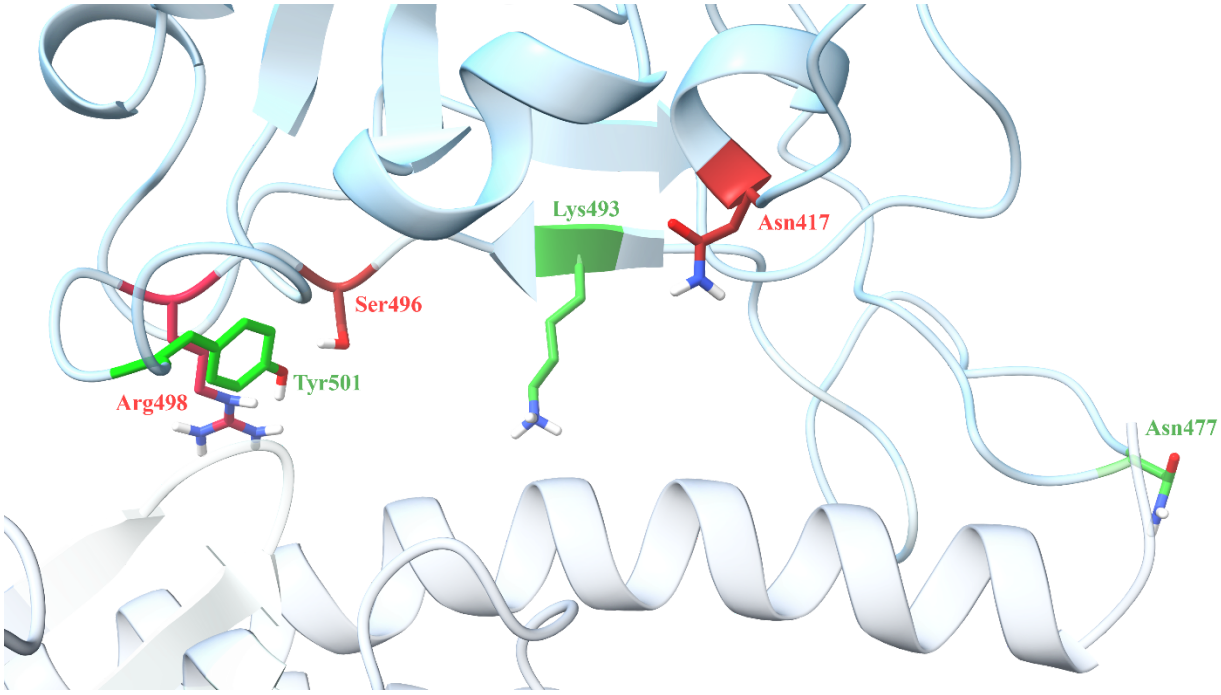

Figure 8. Omicron Q493K SARS-CoV-2 RBD - hACE2 Interactions. Highlighted are residues that most significantly affect binding based upon hydrogen bonding occurrence and pairwise residue decomposition changes in the WT and Omicron variant. Shown in red are mutated residues that display less favorable or less significant interaction. Shown in green are the mutated residues that became more significant for RBD - hACE2 interactions.

SARS-CoV-2 Potential Inhibitors

The goal of this section, in addition to assessing the possible disruption of the interaction caused by ligands bound in the active site, was to analyze the properties and residue interactions significant for the SARS-CoV-2 RBD - hACE2 interaction. Other analyses used to investigate the SARS-CoV-2 RBD and hACE2 complex are discussed in previous sections; however, we decided to perform ten different seeds of 300ns MD simulations to further understand the baseline energetics of the SARS-CoV-2 RBD and hACE2 interaction. The average MM-GBSA binding free energy of the 3 μs trajectory was -31.2 ± 10.6 kcal/mol (Table 7). Additionally, the binding free energies of the individual 10 seeds throughout MD simulations suggest that the SARS-CoV-2 RBD and hACE2 complex sample a variety of structures.

Table 7. MM-GBSA Binding Energies of 1 µs and 3 µs ensemble for SARS-CoV-2 RBD Complexed with hACE2.

6LZG	MM-GBSA Average (kcal/mol)	Std. Dev. (kcal/mol)
3 µs	-31.23	10.55

Additionally, we ran native contact analysis using the concatenated 3 µs ensemble. We identified 299 native contacts in the interface between SARS-CoV-2 and hACE2. The average fraction of native contacts in each frame of the ensemble was 0.94. Figure 7 displays the fraction of native contacts for each frame throughout the simulation. Notably, there is a decrease in the fraction of native contacts between frames 6,493 and 8,550, which occur in seed 3. After visualizing the 3 µs ensemble, we did not identify a noticeable difference in the SARS-CoV-2 RBD and hACE2 interface during these frames.

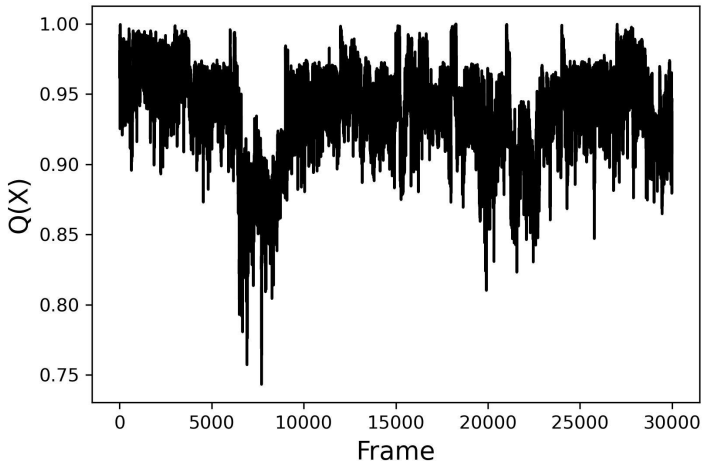

Figure 7. Native Contact Analysis in the Interface of Apo 3 µs Ensemble.

Schrödinger's SiteMap program was used to predict and score potential ligand binding sites based on volume, hydrophilicity/hydrophobicity, and H-bonding ability.[56] Five binding sites were identified on the model, with three displaying favorable SScores and DScores. Sites #1 and #3 appear to flank the ACE2 active site.[57, 58] Site #2, displayed in Figure 8 (SScore 1.002, DScore 1.017), occurs at the hACE2 – SARS-CoV-2 RBD complex junction. This site notably contains

many residues necessary for the formation of this complex.[60, 22] This may suggest the possibility for a ligand to disrupt the ability of the SARS-CoV-2 RBD to complex with hACE2. So, Site #2 was selected for ligand docking calculations. The contribution of the nearby N-glycosylated Asn90 to Site #2 further suggests the possibility that different glycans may affect the favorability of this binding site. Two additional smaller binding sites (Sites #4 and #5) are predicted on the surface of hACE2 for 6LZG. All sites and their properties are detailed in Figure S2 and Table S2.

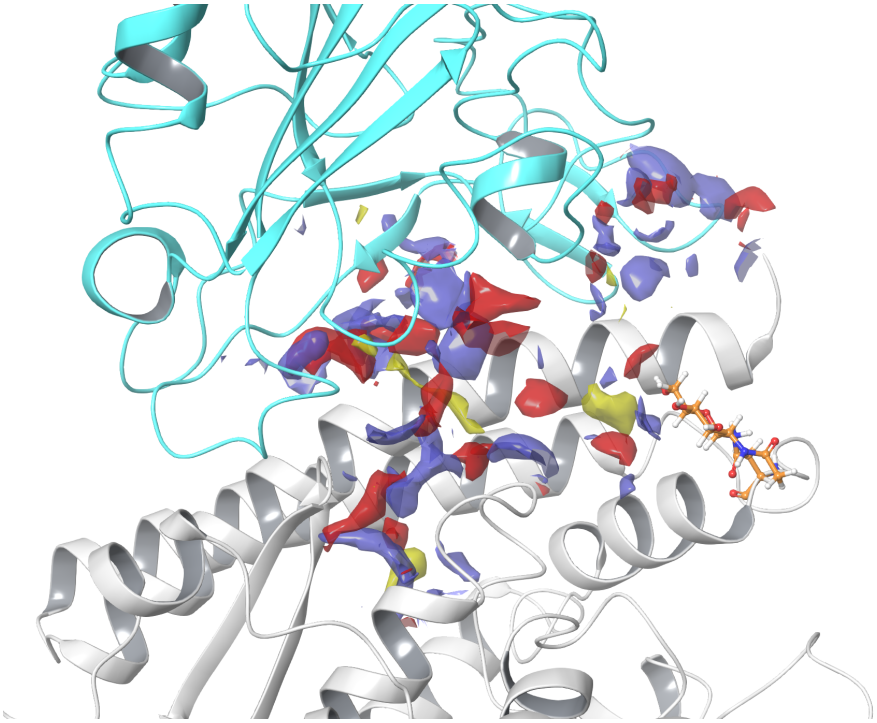

Figure 8. SARS-CoV-2 RBD and hACE2 Interface Binding Site. In the image, hACE2 is shown in white and SARS-CoV-2 RBD is shown in cyan. H-bond accepting sites are colored red, H-bond donating sites are colored blue, and hydrophobic sites are colored yellow. N-linked glycans bound to Asn90 are shown in orange. 6LZG Site #2 was predicted to have a SiteMap SScore of 1.002 and DScore of 1.017. Asn90 is N-glycosylated with NAG.

To determine whether a ligand might favorably bind to Site #2, a small sample of common ACE inhibitors, molecules identified by LSBio as potential SARS-CoV-2 S Protein inhibitors, and diquafosol were screened using Schrödinger's Glide program.[55, 56] In preparation for docking, we determined the proper protonation states of all the ligands at pH 7.4 using

Schrödinger's Epik program. However, the Epik program predicted that the protonation state of Lisinopril had a NH_2^+ on the structure. Unsure of this prediction, we decided to use both Lisinopril structures. All structures, XP GlideScores, and their relative ranking are detailed in Table S3. Of these structures, diquafosol scored most favorably.

Of the 17 ligands screened, results of which are depicted in Tables S3, seven ligands and their three top scoring poses were selected for further analysis in MD simulations based on Glide Scores and their corresponding rank. All diquafosol poses scored higher than the other ligands' poses. The first pose of fosinopril, lisinopril, physcion, and emodin_H11074 (emodin) were the next top scoring poses of all the ligands, respectively. Additionally, the ligand lisinopril, with an overall charge of -1, also scored highly and was selected for further analysis. For this ligand, we were specifically interested to see how the -NH- or -NH_2^+- affected its binding to the interface. Also, as previously mentioned, the Epik program predicted that the backbone nitrogen of lisinopril should be protonated, resulting in -NH_2^+- and a net neutral charge. At a pKa of 7.4, it is possible there would be a mixture of lisinopril with both protonation states (-NH- and -NH_2^+-), so we decided to investigate both. Also, we selected a lower ranked drug, fosinoprilat, for the sake of increasing the diversity of structures. Fosinoprilat was ranked 16th. We visualized the top 3 poses of the ligands selected and decided to run MD simulations on the poses that were visibly distinct.

Before beginning MD simulations, we assessed the pharmacological properties of each ligand using the Schrödinger QikProp ADME program (Table 8). All ligands selected for MD analysis are known drugs in clinical use, so we expected favorable ADME properties. Properties for emodin, fosinopril, fosinoprilat, both lisinoprils, and physcion did not violate the 95% range for known drugs. As mentioned in Table 8, diquafosol exceeds the indicated range for the

properties: molecular weight, H-bond acceptor, and logP octanol/water. This analysis indicates that diquafosol is water soluble, which is further supported given that it is a common compound in eye drops. Additionally, the molecular structure of diquafosol is notably uncommon with four chained phosphate groups, so it is possible that the ADME program is not trained on molecules of similar structures. This is indicated in Table 8 for the properties aqueous solubility and $logIC_{50}$. The ADME program noted that diquafosol exceeds the molecular weight of the drugs that were trained for the aforementioned properties. Additionally, PAINS screenings were conducted on the 7 ligands. The two screenings that were used are mentioned in the methods section. Both screenings found that emodin and physcion did not pass because of the quinone core in both structures. Also, the non-specific activity of both compounds could be due to their numerous pharmacological properties. These results indicate that the binding activity of the other 5 ligands are specific. Overall, from ADME analysis and PAINS screenings we concluded that these 7 ligands are viable compounds for further analysis.

Table 8. ADME Properties for 7 Selected Ligands. ADME properties for diquafosol, emodin, fosinopril, fosinoprilat, lisinopril with $-NH_2^+-$ backbone nitrogen, lisinopril with -NH- backbone nitrogen, and physcion. H-bond donor and acceptor refers to the average number of hydrogen atoms on the molecule that is estimated to be capable of donating or accepting a hydrogen bond, respectively. logP Octanol/Water and logS Aqueous Solubility refers to the solubility of the ligand. logBB Brain/Blood refers to how likely the drug is able to cross the blood brain barrier. Lastly, $logIC_{50}$ HERG K^+ refers to the amount (in log scale) that would need to be taken to block the HERG K^+ channel. Data that exceeds the range of 95% of known drugs used in the ADME program are underlined and data that was flagged due to the molecular weight of the ligand exceeding the trained set of compounds is bolded.

Ligand	Molecular Weight (AMU)	H-Bond Donor	H-Bond Acceptor	logP Octanol/Water	logS Aqueous Solubility	logBB Brain/Blood	$logIC_{50}$ HERG K^+
Diquafosol	<u>790.311</u>	6.000	<u>33.200</u>	<u>-5.404</u>	**0.031**	6.000	**1.064**
Emodin	270.241	1.000	4.250	1.252	-3.051	-1.535	-4.330

Fosinopril	563.670	1.000	12.000	4.677	-5.917	-1.605	-3.374
Fosinoprilat	435.499	1.000	9.000	3.540	-4.264	-1.880	-0.732
Lisinopril (NH_2^+)	405.493	5.000	9.500	-1.209	-1.142	-1.944	-1.828
Lisinopril (NH)	405.493	5.000	9.500	-1.199	-1.080	-1.494	-1.889
Physcion	284.268	0.00	4.250	1.849	-3.978	-1.045	-4.366

Unrestrained MD simulations were conducted on hACE2 - SARS-CoV-2 RBD complexes (6LZG) bound to either diquafosol, emodin, fosinopril, fosinoprilat, lisinopril with both protonation states, or physcion. Distinct poses of each ligand were selected for 100 ns simulations and 5 seeds were conducted for each complex. For the 6LZG ensemble, the MM-GBSA binding free energy analysis is depicted in Tables 9 and 10. The MM-GBSA values in Table 9 represent the binding free energy between the RBD and hACE2 while a drug is present in the interface; suggesting the drug's effect on the RBD-hACE2 interaction. The MM-GBSA binding free energy of the concatenated Apo 3 μs ensemble is -31.23 ± 10.55 kcal/mol.

Table 9. Average MM-GBSA Binding Free Energies between SARS-CoV-2 RBD and hACE2. This energy was estimated in the presence of the bound ligand, i.e. this estimates the binary binding interaction. For each ligand and the corresponding pose the average MM-GBSA value for the RBD - hACE2 interaction, standard deviation, and standard error is reported. Additionally, the ΔΔG is included below, which is the difference in binding free energy of the RBD and hACE2 with a drug bound and the binding free energy between the RBD and hACE2 without a drug present.

Ligand Present in Binding Site	Pose	Avg. ± Std. Dev. (kcal/mol)	Std. Err. (kcal/mol)	ΔΔG (kcal/mol)
Diquafosol	Pose 1	-26.65 ± 9.13	0.13	4.58
	Pose 3	-25.01 ± 11.80	0.17	6.22

Emodin	Pose 1	-22.93 ± 10.21	0.14	8.30
	Pose 2	-27.13 ± 9.81	0.14	4.10
Fosinopril	Pose 1	-25.48 ± 9.31	0.13	5.75
Fosinoprilat	Pose 1	-20.92 ± 9.39	0.13	10.31
	Pose 2	-30.04 ± 9.60	0.14	1.19
	Pose 3	-30.19 ± 9.76	0.14	1.04
Lisinopril (NH_2^+)	Pose 1	-30.26 ± 9.19	0.13	0.97
Lisinopril (NH)	Pose 1	-29.78 ± 9.91	0.14	1.45
Physcion	Pose 1	-24.94 ± 10.58	0.15	6.29
	Pose 2	-23.86 ± 9.65	0.14	7.37
	Pose 3	-34.05 ± 9.60	0.14	-2.82

Our results suggest there is not a significant difference in binding free energy when a drug is present in the interface. Each drug shows a positive increase in the MM-GBSA of the RBD-hACE2 interaction, except for physcion pose 3. This result could suggest that extending the simulations would demonstrate a more significant increase in the RBD and hACE2 binding free energy. Table 10 indicates the binding free energies of the ligand interacting in the interface of the RBD-hACE2 complex. Notably, the binding free energies of fosinopril pose 1, fosinoprilat poses 2 and 3, and lisinopril (both protonation states -NH- and - NH_2^+-) are statistically similar to the binding free energy of the Apo 3 μs ensemble, suggesting that the ligands have a similar strength in interaction. The MM-GBSA binding free energies for both lisinoprils (-NH- and -NH_2^+-) are statistically similar, so for further analysis we decided to continue with the lisinopril structure with the -NH- and negative charge.

Table 10. Average MM-GBSA Binding Free Energies of the Ligand Bound to hACE2-RBD Interface. For each ligand and the corresponding pose the average MM-GBSA value for the interaction of ligand and hACE2-RBD complex, standard deviation, standard error, and percent dissociation is reported. Percent Dissociation was calculated using MM-GBSA value, center of mass analysis and visualization.

Ligand Present in Binding Site	Pose	Avg. ± Std. Dev. (kcal/mol)	Std. Err. (kcal/mol)	Percent Dissociation
Diquafosol	Pose 1	-14.86 ± 15.98	0.23	2.70
	Pose 3	-5.60 ± 23.11	0.33	9.66
Emodin	Pose 1	-10.98 ± 4.77	0.07	33.32
	Pose 2	-14.94 ± 5.68	0.08	4.22
Fosinopril	Pose 1	-24.51 ± 10.67	0.15	11.60
Fosinoprilat	Pose 1	-18.30 ± 8.78	0.12	43.46
	Pose 2	-29.01 ± 11.14	0.16	0.06
	Pose 3	-21.13 ± 12.42	0.18	2.04
Lisinopril (NH_2^+)	Pose 1	-35.05 ± 9.82	0.14	0.26
Lisinopril (NH)	Pose 1	-31.80 ± 11.15	0.16	6.74
Physcion	Pose 1	-10.37 ± 5.07	0.07	82.46
	Pose 2	-12.02 ± 7.99	0.11	72.26
	Pose 3	-10.98 ± 6.28	0.09	77.70

Additionally, Table 10 indicates the percent dissociation of each pose. Percent dissociation signifies the percentage of the concatenated 500 ns simulation when the drug is not in the RBD-hACE2 interface and is not interacting with any amino acids. Notably, diquafosol poses 1 and 3, emodin pose 2, fosinopril pose 1, fosinoprilat poses 2 and 3, and lisinopril (both protonation states -NH- and -NH_2^+-) have relatively low percent dissociations. The percent dissociation for all physcion poses analyzed with MD simulations are above 50%, signifying that

the ligand is not in the binding site for more than half of the simulation. However, after visualizing the simulation, we noticed that physcion still interacts with amino acids on the SARS-CoV-2 RBD or hACE2 receptor outside of the interface. We also looked at the RMSD of all ligand bound complexes to understand the stability of the SARS-CoV-2 RBD and hACE2 complex with a drug present in the interface. Table S4 contains the RMSD graphs for all drug bound complexes with each of the 5 seeds indicated in the legend. The RMSD graphs indicate that physcion seed 3 and seed 4 could be outliers for poses 2 and 3 respectively. However, the RMSD graphs for all other ligands indicate relative convergence between the seeds.

Figure 9 represents both MM-GBSA binding free energies previously mentioned, and the percent dissociation of each ligand pose except physcion (all poses). Notably, the ligands with relatively low percent dissociations did not show a significant decrease in the binding affinity of the interface. However, when the interface binding energy was more positive, the ligand that was present had a relatively high percent dissociation, such as fosinoprilat pose 1 and emodin pose 1, or the ligand had a more positive binding energy with the interface, such as diquafosol poses 1 and 3 and emodin pose 2. This data would suggest that the interaction between hACE2 and SARS-CoV-2 RBD is stronger than the corresponding ligand in the interface.

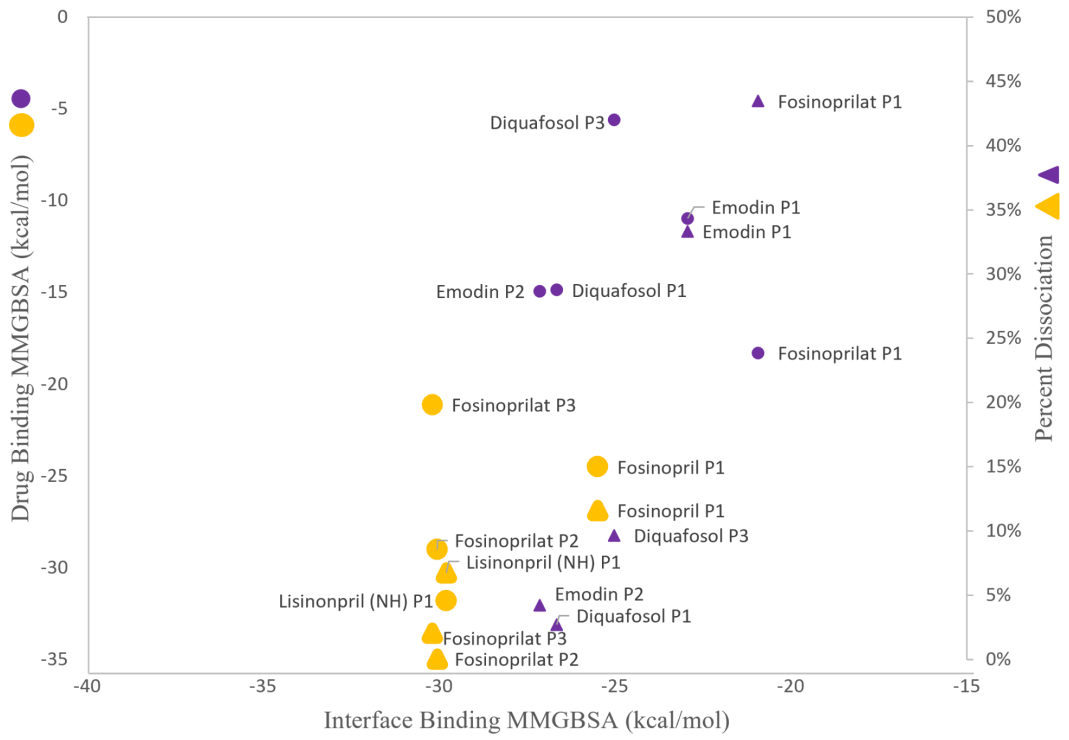

Figure 9. Comparison of MM-GBSA Energies and Percent Dissociation. The x-axis represents the MM-GBSA binding free energies of the RBD-hACE2 interaction with a ligand present in the interface. These points are represented by circles. The y-axis (left side) represents the MM-GBSA binding free energies of the ligand interacting with the RBD-hACE2 complex. The y-axis (right side) represents the percent dissociations. These points are triangles. The larger symbols depicted in orange represent ligands that were selected for further analyses. All other symbols are purple. All ligands, except physcion, are included and labeled next to each data point. Physcion was not included because it appeared to be an outlier once the data was visualized.

Overall, these results suggest that it might be beneficial to further investigate the atomistic interactions of fosinoprilat poses 2 and 3, fosinopril, and lisinopril in the interface. These ligand poses that were selected for further analysis are indicated in Figure 9 in yellow and are depicted in a slightly larger symbol.

Conclusion

In this paper, there are two main focuses: comparison of Omicron and WT SARS-CoV-2

RBD binding affinities and investigating the effects of potential SARS-CoV-2 inhibitors on the interaction between the SARS-CoV-2 RBD and hACE2 receptor. With both research projects we have studied the baseline energetics of the SARS-CoV-2 RBD and hACE2 complex and support that this is a stable interaction.

The Omicron variant of the SARS-CoV-2 virus possesses 32 point mutations, including 15 in the receptor binding domain of the spike protein. Current vaccines produce polyclonal antibodies that target the RBD of the spike protein and prevent the virus from gaining access to human cells. We have utilized classical molecular dynamics to sample the binding behavior of the WT and Omicron spike protein RBD with hACE2 as well as MM-GBSA to compare their binding affinities for hACE2. Remarkably, while we find that the binding affinity between the hACE2 receptor and the WT and Omicron Q493K RBD are similar and within the limits of error of the MM-GBSA binding estimation, the binding for the Omicron Q493R RBD is significantly enhanced. A detailed analysis of the per-residue interaction energies, pairwise decomposition energies, hydrogen-bonding interactions, center-of-mass distance measurements, and clustering suggests that while the Omicron RBD mutations disrupt some favorable WT residue interactions, such mutations also produce new favorable interactions. For instance, for the Q493K RBD, pairwise analysis shows that the Q493K and S477N mutations significantly increase binding whereas K417N, G496S and Q498R reduce binding. For the Q493R RBD, per-residue decomposition analysis indicates that the point mutation confers a significantly larger contribution to favorable binding. For both Omicron RBDs, and in agreement with previous studies, this detailed atomistic analysis points to the importance of 3 residues: Q493K/R, N501Y and S477N.

Additionally, based on our initial analyses of the apo SARS-CoV-2 RBD and hACE2 complex and ligand bound MM-GBSA binding free energy estimates, we determined that ACE inhibitors do not act as effective SARS-CoV-2 RBD inhibitors. This conclusion is primarily based on the interface binding free energies. Specifically, ligands with low percent dissociations do not show a reduction in the binding affinity between the SARS-CoV-2 RBD and the hACE2 receptor, signifying that the ligand isn't significantly disrupting the amino acid interactions present in the interface. However, we believe looking into these ligands further and assessing the individual amino acid interactions can further support our conclusion and possibly lead to potential scaffolds for SARS-CoV-2 RBD inhibitors. Additionally, future studies could consider studying the effect of these ligands on the Omicron RBD and hACE2 interface and comparing how the Omicron mutations affect these inhibitors roles' in disrupting the interface. Based on the previous section, we have shown that the stability and structure of the WT and Omicron SARS-CoV-2 RBD interaction with hACE2 are very similar, but we mention that specific amino acid interactions responsible for maintaining the interface become unfavorable or more favorable. So, using this previous knowledge, it would be interesting to see how the Omicron mutations would affect these potential SARS-CoV-2 inhibitors.

References

1. Wang, C.; Horby, P. W.; Hayden, F. G.; Gao, G. F. A Novel Coronavirus Outbreak of Global Health Concern. *The Lancet* **2020**, *395* (10223), 470–473. https://doi.org/10.1016/S0140-6736(20)30185-9.
2. Pascarella, G.; Strumia, A.; Piliego, C.; Bruno, F.; Buono, R. D.; Costa, F.; Scarlata, S.; Agrò, F. E. COVID-19 Diagnosis and Management: A Comprehensive Review. *Journal of Internal Medicine* **2020**, *288* (2), 192–206. https://doi.org/10.1111/joim.13091.
3. "United States - COVID-19 Overview - Johns Hopkins." Johns Hopkins Coronavirus Resource Center, https://coronavirus.jhu.edu/region/united-states.
4. Berlin, D. A.; Gulick, R. M.; Martinez, F. J. Severe Covid-19 | NEJM. *New England Journal of Medicine* **2020**, *383* (25), 2451–2460.
5. Mittal, A.; Manjunath, K.; Ranjan, R. K.; Kaushik, S.; Kumar, S.; Verma, V. COVID-19 Pandemic: Insights into Structure, Function, and HACE2 Receptor Recognition by SARS-CoV-2. *PLoS Pathog* **2020**, *16* (8). https://doi.org/10.1371/journal.ppat.1008762.
6. Guthrie, G. P. Angiotensin Receptors: Physiology and Pharmacology. *Clinical Cardiology* **1995**, *18* (S3), 29–34. https://doi.org/10.1002/clc.4960181507.
7. Burrell, L. M.; Johnston, C. I.; Tikellis, C.; Cooper, M. E. ACE2, a New Regulator of the Renin–Angiotensin System. *Trends in Endocrinology & Metabolism* **2004**, *15* (4), 166–169. https://doi.org/10.1016/j.tem.2004.03.001.
8. Cruz-Diaz, N.; Wilson, B. A.; Chappell, M. C. *Peptidases and the Renin-Angiotensin System: The Alternative Angiotensin-(1-7) Cascade*; IntechOpen, 2017. https://doi.org/10.5772/65949.
9. Walls, A. C.; Park, Y.-J.; Tortorici, M. A.; Wall, A.; McGuire, A. T.; Veesler, D. Structure, Function, and Antigenicity of the SARS-CoV-2 Spike Glycoprotein. *Cell* **2020**, *181* (2), 281-292.e6. https://doi.org/10.1016/j.cell.2020.02.058.
10. Li, F.; Berardi, M.; Li, W.; Farzan, M.; Dormitzer, P. R.; Harrison, S. C. Conformational States of the Severe Acute Respiratory Syndrome Coronavirus Spike Protein Ectodomain. *J Virol* **2006**, *80* (14), 6794–6800. https://doi.org/10.1128/JVI.02744-05.
11. Guidry, J. P. D.; Laestadius, L. I.; Vraga, E. K.; Miller, C. A.; Perrin, P. B.; Burton, C. W.; Ryan, M.; Fuemmeler, B. F.; Carlyle, K. E. Willingness to Get the COVID-19 Vaccine with and without Emergency Use Authorization. American Journal of Infection Control 2021, 49 (2), 137–142. https://doi.org/10.1016/j.ajic.2020.11.018
12. Krammer, F. SARS-COV-2 Vaccines in Development. Nature 2020, 586 (7830), 516–527. https://doi.org/10.1038/s41586-020-2798-3
13. Mascellino, M. T.; Di Timoteo, F.; De Angelis, M.; Oliva, A. Overview of the Main Anti-SARS-Cov-2 Vaccines: Mechanism of Action, Efficacy and Safety. Infection and Drug Resistance 2021, Volume 14, 3459–3476. https://doi.org/10.2147/IDR.S315727
14. Mascellino, M. T.; Di Timoteo, F.; De Angelis, M.; Oliva, A. Overview of the Main Anti-SARS-Cov-2 Vaccines: Mechanism of Action, Efficacy and Safety. Infection and Drug Resistance 2021, Volume 14, 3459–3476. https://doi.org/10.2147/IDR.S315727
15. Center for Drug Evaluation and Research. Coronavirus (COVID-19): Drugs. https://www.fda.gov/drugs/emergency-preparedness-drugs/coronavirus-covid-19-drugs (accessed Apr 20, 2023).
16. Kulanthaivel, S.; Kaliberdenko, V. B.; Balasundaram, K.; Shterenshis, M. V.; Scarpellini, E.; Abenavoli, L. Tocilizumab in SARS-COV-2 Patients with the Syndrome of Cytokine

Storm: A Narrative Review. Reviews on Recent Clinical Trials 2021, 16 (2), 138–145. 10.2174/1574887115666200917110954

17. Kalil, A. C.; Patterson, T. F.; Mehta, A. K.; Tomashek, K. M.; Wolfe, C. R.; Ghazaryan, V.; Marconi, V. C.; Ruiz-Palacios, G. M.; Hsieh, L.; Kline, S.; Tapson, V.; Iovine, N. M.; Jain, M. K.; Sweeney, D. A.; El Sahly, H. M.; Branche, A. R.; Regalado Pineda, J.; Lye, D. C.; Sandkovsky, U.; Luetkemeyer, A. F.; Cohen, S. H.; Finberg, R. W.; Jackson, P. E. H.; Taiwo, B.; Paules, C. I.; Arguinchona, H.; Erdmann, N.; Ahuja, N.; Frank, M.; Oh, M.-don; Kim, E.-S.; Tan, S. Y.; Mularski, R. A.; Nielsen, H.; Ponce, P. O.; Taylor, B. S.; Larson, L. A.; Rouphael, N. G.; Saklawi, Y.; Cantos, V. D.; Ko, E. R.; Engemann, J. J.; Amin, A. N.; Watanabe, M.; Billings, J.; Elie, M.-C.; Davey, R. T.; Burgess, T. H.; Ferreira, J.; Green, M.; Makowski, M.; Cardoso, A.; de Bono, S.; Bonnett, T.; Proschan, M.; Deye, G. A.; Dempsey, W.; Nayak, S. U.; Dodd, L. E.; Beigel, J. H. Baricitinib Plus Remdesivir for Hospitalized Adults with Covid-19. New England Journal of Medicine 2021, 384 (9), 795–807.
18. Bruxvoort, K. J.; Sy, L. S.; Qian, L.; Ackerson, B. K.; Luo, Y.; Lee, G. S.; Tian, Y.; Florea, A.; Aragones, M.; Tubert, J. E.; Takhar, H. S.; Ku, J. H.; Paila, Y. D.; Talarico, C. A.; Tseng, H. F. Effectiveness of Mrna-1273 against Delta, Mu, and Other Emerging Variants of SARS-COV-2: Test Negative Case-Control Study. BMJ 2021. https://doi.org/10.1136/bmj-2021-068848
19. Tenforde, M. W.; Self, W. H.; Adams, K.; Gaglani, M.; Ginde, A. A.; McNeal, T.; Ghamande, S.; Douin, D. J.; Talbot, H. K.; Casey, J. D.; Mohr, N. M.; Zepeski, A.; Shapiro, N. I.; Gibbs, K. W.; Files, D. C.; Hager, D. N.; Shehu, A.; Prekker, M. E.; Erickson, H. L.; Exline, M. C.; Gong, M. N.; Mohamed, A.; Henning, D. J.; Steingrub, J. S.; Peltan, I. D.; Brown, S. M.; Martin, E. T.; Monto, A. S.; Khan, A.; Hough, C. L.; Busse, L. W.; ten Lohuis, C. C.; Duggal, A.; Wilson, J. G.; Gordon, A. J.; Qadir, N.; Chang, S. Y.; Mallow, C.; Rivas, C.; Babcock, H. M.; Kwon, J. H.; Halasa, N.; Chappell, J. D.; Lauring, A. S.; Grijalva, C. G.; Rice, T. W.; Jones, I. D.; Stubblefield, W. B.; Baughman, A.; Womack, K. N.; Rhoads, J. P.; Lindsell, C. J.; Hart, K. W.; Zhu, Y.; Olson, S. M.; Kobayashi, M.; Verani, J. R.; Patel, M. M. Association between Mrna Vaccination and COVID-19 Hospitalization and Disease Severity. JAMA 2021, 326 (20), 2043. doi:10.1001/jama.2021.19499
20. Shang, J.; Ye, G.; Shi, K.; Wan, Y.; Luo, C.; Aihara, H.; Geng, Q.; Auerbach, A.; Li, F. Structural Basis of Receptor Recognition by SARS-CoV-2. *Nature* **2020**, *581* (7807), 221–224. https://doi.org/10.1038/s41586-020-2179-y.
21. Wang, X.; Yang, C.; Sun, Y.; Sui, X.; Zhu, T.; Wang, Q.; Wang, S.; Yang, J.; Yang, W.; Liu, F.; Zhang, M.; Wang, Y.; Luo, Y. A Novel Screening Strategy of Anti-SARS-CoV-2 Drugs via Blocking Interaction between Spike RBD and ACE2. *Environment International* **2021**, *147*, 106361. https://doi.org/10.1016/j.envint.2020.106361.
22. Wang, Q.; Zhang, Y.; Wu, L.; Niu, S.; Song, C.; Zhang, Z.; Lu, G.; Qiao, C.; Hu, Y.; Yuen, K.-Y.; Wang, Q.; Zhou, H.; Yan, J.; Qi, J. Structural and Functional Basis of SARS-CoV-2 Entry by Using Human ACE2. *Cell* **2020**, *181* (4), 894-904.e9. https://doi.org/10.1016/j.cell.2020.03.045.
23. Maffucci, I.; Contini, A. In Silico Drug Repurposing for SARS-CoV-2 Main Proteinase and Spike Proteins | Journal of Proteome Research. *ACS Publications* **2020**. https://doi.org/10.1021/acs.jproteome.0c00383.

24. Alazmi, M.; Motwalli, O. Molecular Basis for Drug Repurposing to Study the Interface of the S Protein in SARS-CoV-2 and Human ACE2 through Docking, Characterization, and Molecular Dynamics for Natural Drug Candidates. *J Mol Model* **2020**, *26* (12), 338. https://doi.org/10.1007/s00894-020-04599-8.
25. Trezza, A.; Iovinelli, D.; Santucci, A.; Prischi, F.; Spiga, O. An Integrated Drug Repurposing Strategy for the Rapid Identification of Potential SARS-CoV-2 Viral Inhibitors. *Scientific Reports* **2020**, *10* (1), 13866. https://doi.org/10.1038/s41598-020-70863-9.
26. Harvey, W. T.; Carabelli, A. M.; Jackson, B.; Gupta, R. K.; Thomson, E. C.; Harrison, E. M.; Ludden, C.; Reeve, R.; Rambaut, A.; Peacock, S. J.; Robertson, D. L. SARS-COV-2 Variants, Spike Mutations and Immune Escape. Nature Reviews Microbiology 2021, 19 (7), 409–424. https://doi.org/10.1038/s41579-021-00573-0
27. Duchene, S.; Featherstone, L.; Haritopoulou-Sinanidou, M.; Rambaut, A.; Lemey, P.; Baele, G. Temporal Signal and the Phylodynamic Threshold of SARS-COV-2. Virus Evolution 2020, 6 (2). https://doi.org/10.1093/ve/veaa061
28. Gupta, R. K. Will SARS-COV-2 Variants of Concern Affect the Promise of Vaccines? Nature Reviews Immunology 2021, 21 (6), 340–341. https://doi.org/10.1038/s41577-021-00556-5
29. Choi, J. Y.; Smith, D. M. SARS-COV-2 Variants of Concern. Yonsei Medical Journal 2021, 62 (11), 961. https://doi.org/10.3349/ymj.2021.62.11.961
30. Cameroni, E.; Bowen, J. E.; Rosen, L. E.; Saliba, C.; Zepeda, S. K.; Culap, K.; Pinto, D.; VanBlargan, L. A.; De Marco, A.; di Iulio, J.; Zatta, F.; Kaiser, H.; Noack, J.; Farhat, N.; Czudnochowski, N.; Havenar-Daughton, C.; Sprouse, K. R.; Dillen, J. R.; Powell, A. E.; Chen, A.; Maher, C.; Yin, L.; Sun, D.; Soriaga, L.; Bassi, J.; Silacci-Fregni, C.; Gustafsson, C.; Franko, N. M.; Logue, J.; Iqbal, N. T.; Mazzitelli, I.; Geffner, J.; Grifantini, R.; Chu, H.; Gori, A.; Riva, A.; Giannini, O.; Ceschi, A.; Ferrari, P.; Cippà, P. E.; Franzetti-Pellanda, A.; Garzoni, C.; Halfmann, P. J.; Kawaoka, Y.; Hebner, C.; Purcell, L. A.; Piccoli, L.; Pizzuto, M. S.; Walls, A. C.; Diamond, M. S.; Telenti, A.; Virgin, H. W.; Lanzavecchia, A.; Snell, G.; Veesler, D.; Corti, D. Broadly Neutralizing Antibodies Overcome SARS-COV-2 Omicron Antigenic Shift. Nature 2021, 602 (7898), 664–670. https://doi.org/10.1038/s41586-021-04386-2
31. Zhang, X.; Wu, S.; Wu, B.; Yang, Q.; Chen, A.; Li, Y.; Zhang, Y.; Pan, T.; Zhang, H.; He, X. SARS-COV-2 Omicron Strain Exhibits Potent Capabilities for Immune Evasion and Viral Entrance. Signal Transduction and Targeted Therapy 2021, 6 (1). https://doi.org/10.1038/s41392-021-00852-5
32. Han, P.; Li, L.; Liu, S.; Wang, Q.; Zhang, D.; Xu, Z.; Han, P.; Li, X.; Peng, Q.; Su, C.; Huang, B.; Li, D.; Zhang, R.; Tian, M.; Fu, L.; Gao, Y.; Zhao, X.; Liu, K.; Qi, J.; Gao, G. F.; Wang, P. Receptor Binding and Complex Structures of Human ACE2 to Spike RBD from Omicron and Delta SARS-COV-2. Cell 2022, 185 (4). https://doi.org/10.1016/j.cell.2022.01.001
33. Chan, K. K.; Dorosky, D.; Sharma, P.; Abbasi, S. A.; Dye, J. M.; Kranz, D. M.; Herbert, A. S.; Procko, E. Engineering Human ACE2 to Optimize Binding to the Spike Protein of SARS Coronavirus 2. Science 2020, 369 (6508), 1261–1265.
34. Cui, Z.; Liu, P.; Wang, N.; Wang, L.; Fan, K.; Zhu, Q.; Wang, K.; Chen, R.; Feng, R.; Jia, Z.; Yang, M.; Xu, G.; Zhu, B.; Fu, W.; Chu, T.; Feng, L.; Wang, Y.; Pei, X.; Yang, P.; Xie, X. S.; Cao, L.; Cao, Y.; Wang, X. Structural and Functional Characterizations of

Infectivity and Immune Evasion of SARS-COV-2 Omicron. Cell 2022, 185 (5). https://doi.org/10.1016/j.cell.2022.01.019
35. Wu, L.; Zhou, L.; Mo, M.; Liu, T.; Wu, C.; Gong, C.; Lu, K.; Gong, L.; Zhu, W.; Xu, Z. SARS-COV-2 Omicron RBD Shows Weaker Binding Affinity than the Currently Dominant Delta Variant to Human ACE2. Signal Transduction and Targeted Therapy 2022, 7 (1). https://doi.org/10.1038/s41392-021-00863-2
36. Nguyen, H. L.; Thai, N. Q.; Nguyen, P. H.; Li, M. S. SARS-COV-2 Omicron Variant Binds to Human Cells More Strongly than the Wild Type: Evidence from Molecular Dynamics Simulation. The Journal of Physical Chemistry B 2022, 126 (25), 4669–4678. https://doi.org/10.1021/acs.jpcb.2c01048
37. da Costa, C. H.; de Freitas, C. A.; Alves, C. N.; Lameira, J. Assessment of Mutations on RBD in the Spike Protein of SARS-COV-2 Alpha, Delta and Omicron Variants. Scientific Reports 2022, 12 (1). https://doi.org/10.1038/s41598-022-12479-9
38. Kumar, R.; Murugan, N. A.; Srivastava, V. Improved Binding Affinity of Omicron's Spike Protein for the Human Angiotensin-Converting Enzyme 2 Receptor Is the Key behind Its Increased Virulence. International Journal of Molecular Sciences 2022, 23 (6), 3409. https://doi.org/10.3390/ijms23063409
39. Berman, H. M. The Protein Data Bank. Nucleic Acids Research 2000, 28 (1), 235–242. https://doi.org/10.1093/nar/28.1.235
40. Schrödinger Release 2019-3: Protein Preparation Wizard; Epik, Schrödinger, LLC: New York, NY, 2016. Impact, Schrödinger, LLC, New York, NY, 2016; Prime, Schrödinger, LLC, New York, NY, 2019.
41. Søndergaard, C. R.; Olsson, M. H. M.; Rostkowski, M.; Jensen, J. H., Improved Treatment of Ligands and Coupling Effects in Empirical Calculation and Rationalization of pKa Values. Journal of Chemical Theory and Computation 2011, 7 (7), 2284-2295.
42. Olsson, M. H. M.; Søndergaard, C. R.; Rostkowski, M.; Jensen, J. H., PROPKA3: Consistent Treatment of Internal and Surface Residues in Empirical pKa Predictions. Journal of Chemical Theory and Computation 2011, 7 (2), 525-537.
43. Harder, E.; Damm, W.; Maple, J.; Wu, C.; Reboul, M.; Xiang, J. Y.; Wang, L.; Lupyan, D.; Dahlgren, M. K.; Knight, J. L.; Kaus, J. W.; Cerutti, D. S.; Krilov, G.; Jorgensen, W. L.; Abel, R.; Friesner, R. A., OPLS3: A Force Field Providing Broad Coverage of Drug-like Small Molecules and Proteins. J Chem Theory Comput 2016, 12 (1), 281-96.
44. D.A. Case, I. Y. B.-S., S.R. Brozell, D.S. Cerutti, T.E. Cheatham, III, V.W.D. Cruzeiro, T.A. Darden, R.E. Duke, D. Ghoreishi, M.K. Gilson, H. Gohlke, A.W. Goetz, D. Greene, R Harris, N. Homeyer, S. Izadi, A. Kovalenko, T. Kurtzman, T.S. Lee, S. LeGrand, P. Li, C. Lin, J. Liu, T. Luchko, R. Luo, D.J. Mermelstein, K.M. Merz, Y. Miao, G. Monard, C. Nguyen, H. Nguyen, I. Omelyan, A. Onufriev, F. Pan, R. Qi, D.R. Roe, A. Roitberg, C. Sagui, S. Schott-Verdugo, J. Shen, C.L. Simmerling, J. Smith, R. Salomon-Ferrer, J. Swails, R.C. Walker, J. Wang, H. Wei, R.M. Wolf, X. Wu, L. Xiao, D.M. York and P.A. Kollman, AMBER 2018, University of California, San Francisco, 2018.
45. Götz, A. W.; Williamson, M. J.; Xu, D.; Poole, D.; Le Grand, S.; Walker, R. C., Routine Microsecond Molecular Dynamics Simulations with AMBER on GPUs. 1. Generalized Born. Journal of chemical theory and computation 2012, 8 (5), 1542-1555.
46. Salomon-Ferrer, R.; Götz, A. W.; Poole, D.; Le Grand, S.; Walker, R. C., Routine Microsecond Molecular Dynamics Simulations with AMBER on GPUs. 2. Explicit

Solvent Particle Mesh Ewald. Journal of Chemical Theory and Computation 2013, 9 (9), 3878-3888.
47. Kirschner, K. N.; Yongye, A. B.; Tschampel, S. M.; González-Outeiriño, J.; Daniels, C. R.; Foley, B. L.; Woods, R. J. Glycam06: A Generalizable Biomolecular Force Field. Carbohydrates. Journal of Computational Chemistry 2007, 29 (4), 622–655. https://doi.org/10.1002/jcc.20820
48. Maier, J. A.; Martinez, C.; Kasavajhala, K.; Wickstrom, L.; Hauser, K. E.; Simmerling, C., ff14SB: Improving the Accuracy of Protein Side Chain and Backbone Parameters from ff99SB. Journal of chemical theory and computation 2015, 11 (8), 3696-3713.
49. Wang, J.; Wang, W.; Kollman, P. A.; Case, D. A., Automatic atom type and bond type perception in molecular mechanical calculations. Journal of Molecular Graphics and Modelling 2006, 25 (2), 247-260
50. Jakalian, A.; Jack, D. B.; Bayly, C. I., Fast, efficient generation of high-quality atomic charges. AM1-BCC model: I. Method. Journal of Computational Chemistry 2000, 21 (2), 132-146.
51. Miller, B. R.; McGee, T. D.; Swails, J. M.; Homeyer, N.; Gohlke, H.; Roitberg, A. E., MMPBSA.py: An Efficient Program for End-State Free Energy Calculations. Journal of Chemical Theory and Computation 2012, 8 (9), 3314-3321.
52. Halgren, T. A., Identifying and Characterizing Binding Sites and Assessing Druggability. Journal of Chemical Information and Modeling 2009, 49 (2), 377-389.
53. Wang, J.; Wolf, R. M.; Caldwell, J. W.; Kollman, P. A.; Case, D. A., Development and testing of a general amber force field. Journal of Computational Chemistry 2004, 25 (9), 1157-1174.
54. Hanwell, M. D.; Curtis, D. E.; Lonie, D. C.; Vandermeersch, T.; Zurek, E.; Hutchison, G. R., Avogadro: an advanced semantic chemical editor, visualization, and analysis platform. Journal of Cheminformatics 2012, 4 (1), 17.
55. Friesner, R. A.; Banks, J. L.; Murphy, R. B.; Halgren, T. A.; Klicic, J. J.; Mainz, D. T.; Repasky, M. P.; Knoll, E. H.; Shelley, M.; Perry, J. K.; Shaw, D. E.; Francis, P.; Shenkin, P. S., Glide: A New Approach for Rapid, Accurate Docking and Scoring. 1. Method and Assessment of Docking Accuracy. Journal of Medicinal Chemistry 2004, 47 (7), 1739-1749.
56. Halgren, T. A.; Murphy, R. B.; Friesner, R. A.; Beard, H. S.; Frye, L. L.; Pollard, W. T.; Banks, J. L., Glide: A New Approach for Rapid, Accurate Docking and Scoring. 2. Enrichment Factors in Database Screening. Journal of Medicinal Chemistry 2004, 47 (7), 1750-1759.
57. Guo, H.; Gao, Y.; Li, T.; Li, T.; Lu, Y.; Zheng, L.; Liu, Y.; Yang, T.; Luo, F.; Song, S.; Wang, W.; Yang, X.; Nguyen, H. C.; Zhang, H.; Huang, A.; Jin, A.; Yang, H.; Rao, Z.; Ji, X. Structures of Omicron Spike Complexes and Implications for Neutralizing Antibody Development. Cell Reports 2022, 39 (5), 110770.
58. Guy, J. L.; Jackson, R. M.; Acharya, K. R.; Sturrock, E. D.; Hooper, N. M.; Turner, A. J., Angiotensin-Converting Enzyme-2 (ACE2): Comparative Modeling of the Active Site, Specificity Requirements, and Chloride Dependence. Biochemistry 2003, 42 (45), 13185-13192.
59. Guy, J. L.; Jackson, R. M.; Jensen, H. A.; Hooper, N. M.; Turner, A. J., Identification of critical active-site residues in angiotensin-converting enzyme-2 (ACE2) by site-directed mutagenesis. The FEBS Journal 2005, 272 (14), 3512-3520

60. Shang, J.; Ye, G.; Shi, K.; Wan, Y.; Luo, C.; Aihara, H.; Geng, Q.; Auerbach, A.; Li, F., Structural basis of receptor recognition by SARS-CoV-2. Nature 2020, 581 (7807), 221-224.
61. Goddard, T. D.; Huang, C. C.; Meng, E. C.; Pettersen, E. F.; Couch, G. S.; Morris, J. H.; Ferrin, T. E. UCSF Chimerax: Meeting Modern Challenges in Visualization and Analysis. Protein Science 2017, 27 (1), 14–25. https://doi.org/10.1002/pro.3235
62. Pettersen, E. F.; Goddard, T. D.; Huang, C. C.; Couch, G. S.; Greenblatt, D. M.; Meng, E. C.; Ferrin, T. E. UCSF Chimera?a Visualization System for Exploratory Research and Analysis. Journal of Computational Chemistry 2004, 25 (13), 1605–1612. https://doi.org/10.1002/jcc.20084
63. Best, R. B.; Hummer, G.; Eaton, W. A. Native Contacts Determine Protein Folding Mechanisms in Atomistic Simulations. Proceedings of the National Academy of Sciences 2013, 110 (44), 17874–17879. https://doi.org/10.1073/pnas.1311599110
64. Geng, Q.; Shi, K.; Ye, G.; Zhang, W.; Aihara, H.; Li, F. Structural Basis for Human Receptor Recognition by SARS-COV-2 Omicron Variant BA.1. Journal of Virology 2022, 96 (8). https://doi.org/10.1128/jvi.00249-22
65. Schubert, M.; Bertoglio, F.; Steinke, S.; Heine, P. A.; Ynga-Durand, M. A.; Maass, H.; Sammartino, J. C.; Cassaniti, I.; Zuo, F.; Du, L.; Korn, J.; Milošević, M.; Wenzel, E. V.; Krstanović, F.; Polten, S.; Pribanić-Matešić, M.; Brizić, I.; Baldanti, F.; Hammarström, L.; Dübel, S.; Šustić, A.; Marcotte, H.; Strengert, M.; Protić, A.; Piralla, A.; Pan-Hammarström, Q.; Čičin-Šain, L.; Hust, M. Human Serum from SARS-COV-2-Vaccinated and COVID-19 Patients Shows Reduced Binding to the RBD of SARS-COV-2 Omicron Variant. BMC Medicine 2022, 20 (1). https://doi.org/10.1186/s12916-022-02312-5

Supporting Information

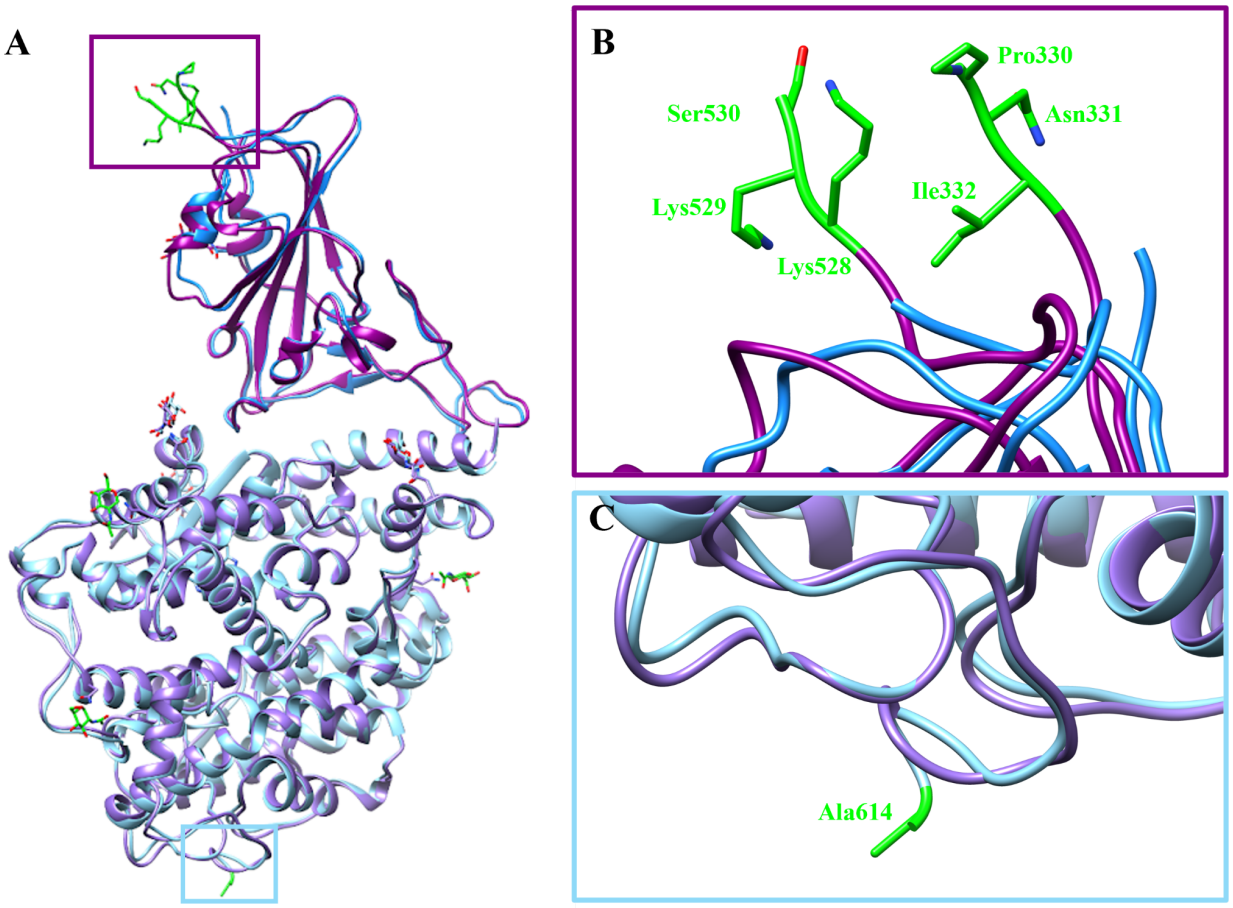

Figure S1. Comparison of the 6LZG and 7WSA Structures. The 6LZG structure is in blue with the RBD depicted in dark blue and the hACE2 receptor depicted in light blue. The 7WSA structure is in purple with the RBD depicted in dark purple and the hACE2 receptor depicted in light purple. The additional residues that were only found on the 6LZG model or the 7WSA model are depicted in green. **[A]** The entire 6LZG and 7WSA structures. In green the additional NAG glycans are shown on the 7WSA structure bound to Asn103, Asn432, and Asn546. **[B]** Additional residues on the beginning (Pro330, Asn331, and Ile332) and end (Lys528, Lys529, and Ser530) of the 7WSA RBD structure. **[C]** The additional residue on the 6LZG hACE2 structure (Ala614).

Table S1. WT and Omicron SARS-CoV-2 RBD Per-residue Decomposition Energies. These energies account for the RBD interaction with hACE2. Each energy is reported as an average over the concatenated 2 μs ensemble. Only the per-residue decomposition energies that are more negative than -1 kcal/mol are listed. Omicron mutated residues are shown in red.

SARS-CoV-2 RBD WT Residue	Per-residue Decomp. (avg. ± std. dev.) (kcal/mol)	SARS-CoV-2 RBD Omicron Q493K Residues	Per-residue Decomp. (avg. ± std. dev.) (kcal/mol)	SARS-CoV-2 RBD Omicron Q493R Residues	Per-residue Decomp. (avg. ± std. dev.) (kcal/mol)
Tyr505	-4.92 ± 0.98	Tyr501	-6.69 ± 1.17	Arg493	-9.86 ± 3.49
Gln493	-4.60 ± 1.90	Lys493	-5.30 ± 2.62	Tyr501	-6.46 ± 1.15
Phe486	-3.30 ± 0.96	Phe486	-3.32 ± 0.99	Phe486	-3.34 ± 0.91
Phe456	-3.00 ± 0.56	His505	-3.09 ± 1.32	His505	-3.33 ± 1.61
Gln498	-2.98 ± 3.21	Phe456	-2.79 ± 0.55	Phe456	-2.75 ± 0.51
Asn501	-2.05 ± 1.19	Tyr489	-2.14 ± 0.70	Tyr489	-2.05 ± 0.67
Tyr489	-1.99 ± 0.71	Leu455	-1.74 ± 0.43	Leu455	-1.82 ± 0.46
Leu455	-1.74 ± 0.37	Ala475	-1.69 ± 1.03	Ala475	-1.64 ± 1.03
Gly502	-1.66 ± 0.49	Thr500	-1.53 ± 0.80	Ser496	-1.59 ± 1.13
Gly496	-1.65 ± 1.14	Ser496	-1.46 ± 1.10	Thr500	-1.39 ± 0.84
Asn487	-1.44 ± 0.92	Asn487	-1.30 ± 0.82	Asn487	-1.33 ± 0.82
Ala475	-1.41 ± 1.00	Gly502	-1.28 ± 0.49	Gly502	-1.31 ± 0.48
Thr500	-1.36 ± 0.86	Asn477	-1.10 ± 1.15	Asn477	-1.02 ± 1.17
Tyr449	-1.35 ± 1.00				

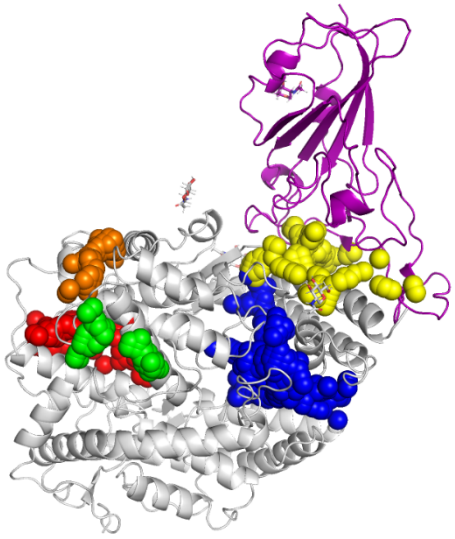

Figure S2. SiteMap Results for 6LZG. Blue indicates Site #1 (SScore 1.005, DScore 1.029), yellow indicates Site #2 (SScore 1.002, DScore 1.017), red indicates Site #3 (SScore 1.053, DScore 1.061), green indicates Site #4 (SScore 0.743, DScore 0.742), and orange indicates Site #5 (SScore 0.696, DScore 0.672). Site #2 occurs in the hACE2 – SARS-CoV-2 RBD complex junction and is the binding site of interest.

Table S2. SiteMap Properties for 6LZG Binding Sites.

Site #	Size	Volume	Exposure	Enclosure	Contact	Phobic	Philic	Balance	Don/Acc
1	251	885.28	0.645	0.696	0.352	0.352	1.010	0.348	1.088
2	164	568.35	0.697	0.702	0.854	0.236	1.057	0.223	0.711
3	133	463.74	0.567	0.777	1.008	0.712	1.060	0.672	0.831
4	56	120.05	0.735	0.546	0.685	0.225	0.887	0.254	0.948
5	50	117.65	0.725	0.549	0.737	0.156	0.989	0.158	1.392

Table S3. Drug Structures and Glide Scores. Ranking for each model is based on XP Glide Score of first pose.

Drug Name	6LZG	
	Glide Score (kcal/mol)	Rank
Benazepril	-4.154	8
Captopril	-3.588	13
Enalapril	-4.097	9
Fosinopril	-6.050	2
Fosinoprilat	-3.287	16
Lisinopril	-4.959	3
Lisinopril (-1)	-3.353	15
Perindopril	-3.569	14
Quinapril	-3.984	11
Ramipril	-4.070	10
Trandolapril	-3.643	12
Aloe Emodin LS-H15204	-4.384	7
Camostat LS-H6976	-2.731	17
Emodin LS-H11074	-4.706	5
Emodin LS-H17409	-4.402	6
Physcion LS-H9395	-4.737	4
Diquafosol	-9.138	1

Table S4. RMSD For All Drug Bound Complexes.

Ligands	Pose 1	Pose 2	Pose 3
Diquafosol	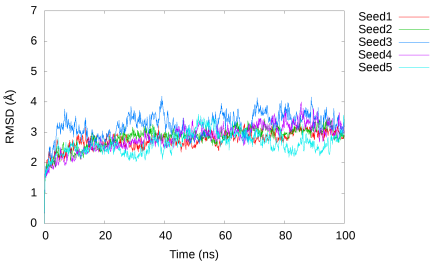	-	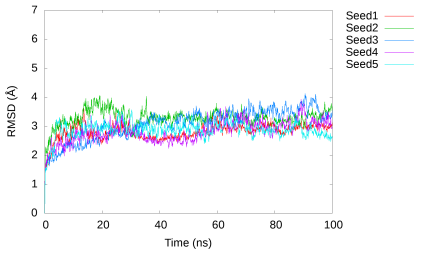

Emodin_H1 1074	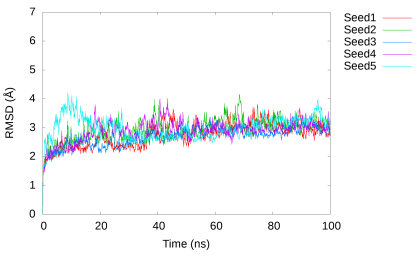	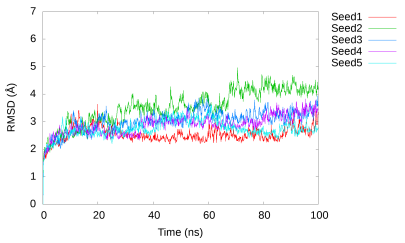	-
Fosinopril	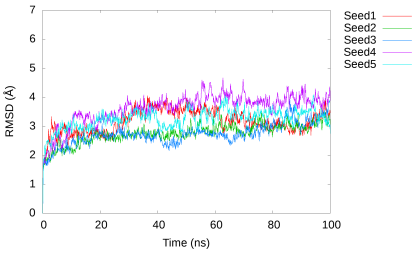	-	-
Fosinoprilat	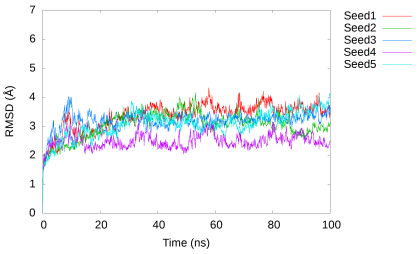	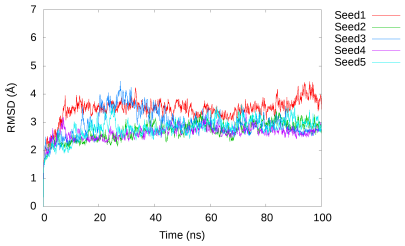	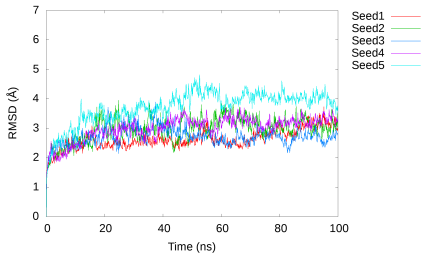
Lisinopril (NH_2^+)	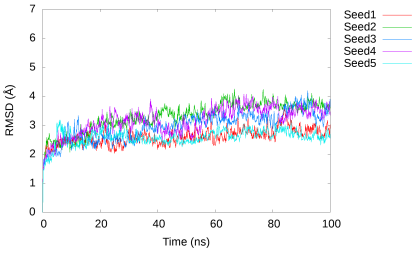	-	-
Lisinopril (NH)	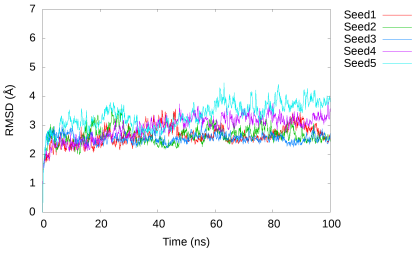	-	-

Physcion	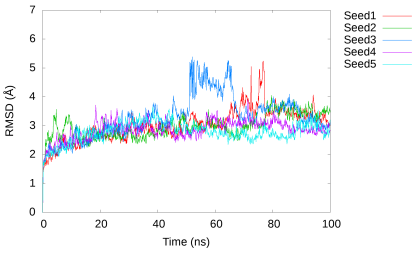 RMSD (Å) Time (ns) Seed1 Seed2 Seed3 Seed4 Seed5	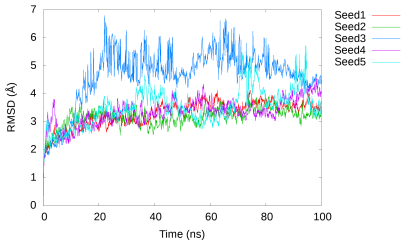 RMSD (Å) Time (ns) Seed1 Seed2 Seed3 Seed4 Seed5	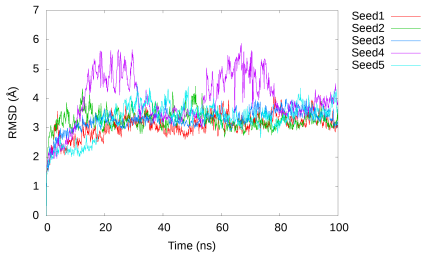 RMSD (Å) Time (ns) Seed1 Seed2 Seed3 Seed4 Seed5